Synapses

Edited by W. Maxwell Cowan,
Thomas C. Südhof, and Charles F. Stevens

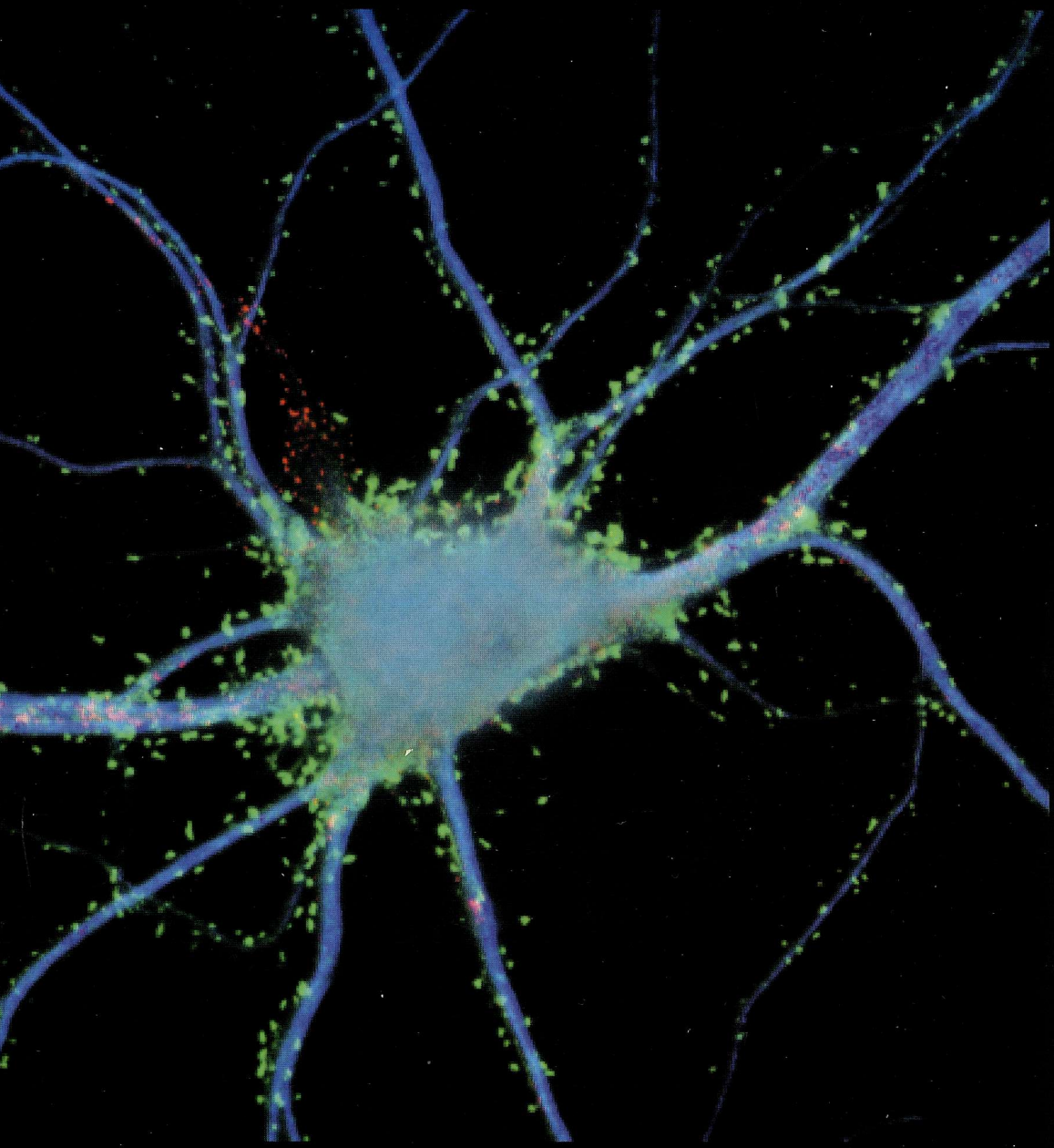

15 Synaptic Variability

New Insights from Reconstructions and Monte Carlo Simulations with MCell

Joel R. Stiles, Thomas M. Bartol, Miriam M. Salpeter, Edwin E. Salpeter, and Terrence J. Sejnowski

Biological structures show tremendous complexity and diversity at the subcellular level. For example, a single cubic millimeter of the cerebral cortex may contain on the order of five billion interdigitated synapses of different shapes and sizes.[1] Subcellular communication is based on a wide variety of chemical signaling pathways, and for synaptic transmission these include neurotransmitter and neuromodulator molecules, proteins involved with exo- and endocytosis, receptor proteins, transport proteins, and oxidative and hydrolytic enzymes. Synaptic crosstalk may result when ligand molecules released from one synapse diffuse to another (Clements, 1996; Barbour and Hausser, 1997; Rusakov and Kullmann, 1998; Rusakov et al., 1999), so the range over which ligands can act likely extends from nanometers to microns. In addition, chemical and structural plasticity at synapses undoubtedly contributes to information storage and processing, and it is widely discussed in relation to high-level cognitive functions such as learning and memory (Edwards, 1995a,b; see Grimwood et al., this volume).

Theoretical studies of ligand diffusion and chemical reaction have been used to investigate synaptic structure-function relationships since the late 1950s (Eccles and Jaeger, 1958), but until recently computer hardware and software limitations have precluded highly realistic three-dimensional (3-D) simulations of reconstructed synapses. As a result the contribution of actual ultrastructure to synaptic current variability (or other signaling phenomena) has gone largely unexplored, and quantitative modeling of synaptic physiology has been severely hampered. Computer hardware limitations have now been significantly overcome by massively parallel systems and, on a smaller scale, by affordable multiprocessor workstations with large amounts of memory and fast graphics-handling capabilities. The major remaining bottleneck is the development of programs that not only provide the requisite simulation capabilities but also interface smoothly with interactive 3-D reconstruction and animation programs. We describe here a program that opens up the study of synapses with realistic geometries at the subcellular level.

Our simulation program, MCell,[2] is based on Monte Carlo (MC) algorithms and incorporates highly realistic 3-D reconstructions into models of ligand diffusion (e.g., neurotransmitter exocytosis) and signaling (e.g., synaptic currents). As shown in Fig. 15.1, MCell simulations are positioned at a biological scale above molecular dynamics but below whole-cell and network modeling studies. Its structural realism lies between the space-filled atomic resolution of molecular dynamics (e.g., AMBER or CHARMM simulations; Cornell et al., 1995; MacKerell et al., 1998) and that of less structure-dependent approaches, such as proteomics (e.g., E-CELL simulations; Tomita et al., 1999) and compartmental models of "Hodgkin-Huxley"–style neurons (e.g., NEURON or GENESIS simulations; Hines, 1993; Bower and Beeman, 1995). In a compartmental model, the complex geometry of an individual cell is subdivided into approximately isopotential parts, each of which becomes a resistive-capacitive element in a branched electrical circuit representation. The actual 3-D

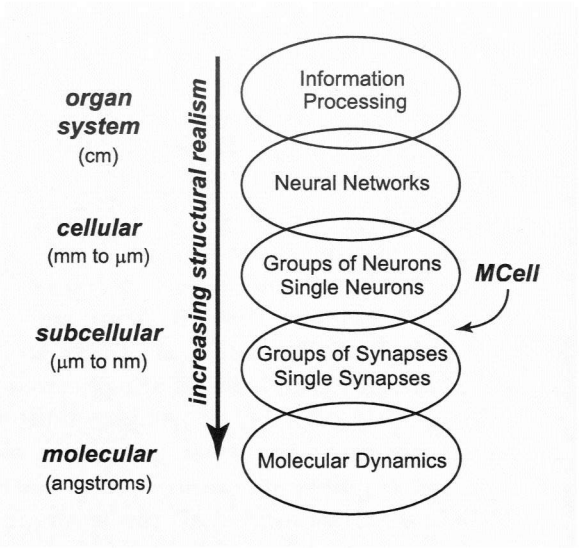

Figure 15.1. Physical scales versus structural realism in computational neuroscience models. MCell simulations encompass diffusion and chemical reaction of molecules in 3-D reconstructions and hence are situated between compartmental models of single- or multiple-neuron excitation and molecular dynamics models of single-molecule structure.

configuration of the neuron(s) and surrounding tissue volume is not explicitly considered, nor is the molecular nature of various conductances and currents that can be incorporated into different compartments. MCell and these other modeling approaches are mostly complementary, and integration of the various approaches is an important direction for future research.

In MCell simulations, the diffusion of individual ligand molecules within a reconstructed 3-D environment is simulated using a Brownian dynamics random walk algorithm, and bulk solution rate constants are converted into MC probabilities so that the diffusing ligands can interact stochastically with individual binding sites, such as receptor proteins, enzymes, and transporters. Such methods can be applied to many questions related to synaptic transmission, such as:

1. How does the architecture of the synaptic cleft affect quantal and multiquantal current amplitudes and time courses at central and peripheral synapses?
2. How do the kinetics and precise localization of transmitter release, receptors, and reuptake sites influence current variability and crosstalk between synapses?
3. How might intra- and extracellular ion fluxes from repeated synaptic activation in realistic synaptic architectures, together with discrete transmembrane conductances and pumps, influence particular regions of neuropil?

4. How do the many calcium-binding proteins in 3-D subcellular microenvironments trigger and regulate a multitude of signaling pathways?

We begin this chapter with a short historical look at the vertebrate neuromuscular junction (NMJ), which has long served as a model synapse for investigations of structure and function. We then review our modeling approach, validate the latest algorithms, and discuss factors that affect numerical accuracy. MCell is used to simulate acetylcholine (ACh) exocytosis at the NMJ and to show how realistic synaptic architecture may account for a significant fraction of miniature endplate current (MEPC) variability. We conclude by describing future directions for continued synaptic reconstruction, simulation, and combined theoretical and experimental studies.

Historical Overview of Structure and Function at the Vertebrate Neuromuscular Junction

The vertebrate NMJ has long served as a model synapse owing to its easy accessibility, large size, and singular distribution. A wealth of physiological and morphological data is available, and, in spite of its unique characteristics, the NMJ has provided many insights into our understanding of central synapses.

Basic features of the NMJ on vertebrate twitch fibers were first described in the 1840s (Doyere, 1840), yet the modern view of NMJ organization began with Couteaux in the 1940s. In a series of illuminating articles, he identified the postjunctional muscle surface as a unique palisade-like specialization rich in acetylcholinesterase (AChE), which is now known as the junctional folds (JFs). Couteaux also helped clarify the relationship between Schwann cells and the NMJ. From him came some of the best early descriptions of the morphology of the vertebrate NMJ, as well as a fascinating view of some early controversies (e.g., Couteaux, 1946, 1955, 1958). However, the detailed morphology of the NMJ was not revealed until the advent of transmission electron microscopy (TEM) in the 1950s and 1960s.

It is now clear that chemically transmitting synapses like the NMJ consist of three distinct compartments: (1) the presynaptic nerve terminal, containing large numbers of synaptic vesicles, numerous mitochondria, and one or more active zones (thickened presynaptic membrane); (2) the postsynaptic apparatus, characterized in part by a dense membrane with an underlying filamentous cytoskeleton; and (3) an intervening synaptic cleft that at the NMJ contains basal lamina material.

A major difference between neuroneuronal synapses and the NMJ is the organization of the second and third compartments. The postsynaptic membrane of the NMJ often is extensively folded, forming JFs of variable depth (generally 0.5–1 μm). These JFs create secondary extracellular cleft spaces connected to the primary cleft, which lies between

the nerve terminal membrane and the tops of the folds. For neuro-neuronal synapses the width of the synaptic cleft is about 10–20 nm, while for the NMJ it is about 50 nm in both the primary and secondary cleft spaces. The overall organization of NMJs on typical vertebrate twitch fibers is shown in Fig. 15.2. The primary and secondary clefts contain AChE active sites and basal lamina proteins, and the latter are part of a complex scaffold that connects neural and musculocytoskeletal elements (Froehner, 1986; Hall and Sanes, 1993; Matsumura and Campbell, 1994; Apel and Merlie, 1995; Sanes and Lichtman, 1999).

Small round vesicles (circa 50 nm in diameter; Fig. 15.2B) were seen in the presynaptic terminals in the first TEM images (Palade and Palay, 1954; Reger, 1955; Robertson, 1956). The anatomical description of synaptic vesicles coincided with physiological studies showing that excitation at the NMJ occurs in multiples of quantal depolarizing events (del Castillo and Katz, 1954). This led to the suggestion that synaptic vesicles contain neurotransmitter molecules that are released by fusion of vesicles with the presynaptic membrane, and that there is a one-to-one correspondence between the release of a single vesicle's contents and a quantal physiological signal. Numerous studies were undertaken in the 1950s and 1960s using biochemical (DeRobertis et al., 1961; Whitaker, 1965), physiological, and electron microscopic (EM; Ceccarelli et al., 1973; Heuser and Reese, 1973) techniques, which supported the claim that vesicles contain the releasable pool of ACh. In addition, the TEM visualization of "omega figures" in fast-frozen tissue (Ceccarelli et al., 1973; Heuser and Reese, 1973)—vesicles fused to the presynaptic membrane by means of an open pore—finally convinced many investigators that ACh is released by exocytosis of quantal packets from synaptic vesicles.

The JFs were initially thought necessary to increase the muscle's postsynaptic receptive surface area. This idea was supported by the proposed mosaic model of acetylcholine receptor (AChR) and AChE distribution (Barnard et al., 1971; Porter et al., 1973). However, the mosaic model was suspect on physiological and theoretical grounds, because it seemed unlikely that many ACh molecules would reach AChRs at the bottom of the JFs during the rising phase of an MEPC. EM autoradiography finally provided direct evidence that AChRs are, in fact, highly concentrated on the crests (i.e., the top 200–300 nm) of the JFs and are present at decreasing average density along the depth of the JF, with essentially none at the bottom (Salpeter et al., 1984). High AChR density therefore is spatially correlated with the presence of the postsynaptic membrane density, which also is mostly observed at the crests of JFs (Fig. 15.2B; Albuquerque et al., 1974; Fertuck and Salpeter, 1974, 1976). Another important result provided by EM autoradiography is that AChE active sites are distributed throughout the primary and secondary cleft spaces, but at average densities much lower than that for the crest AChRs (Salpeter, 1967, 1969; Rogers et al., 1969; Anglister et al., 1994). The high ratio of AChR- to AChE-binding sites at the receptive surface gave rise to the "saturated disc" model of MEPC generation (Matthews-Bellinger and

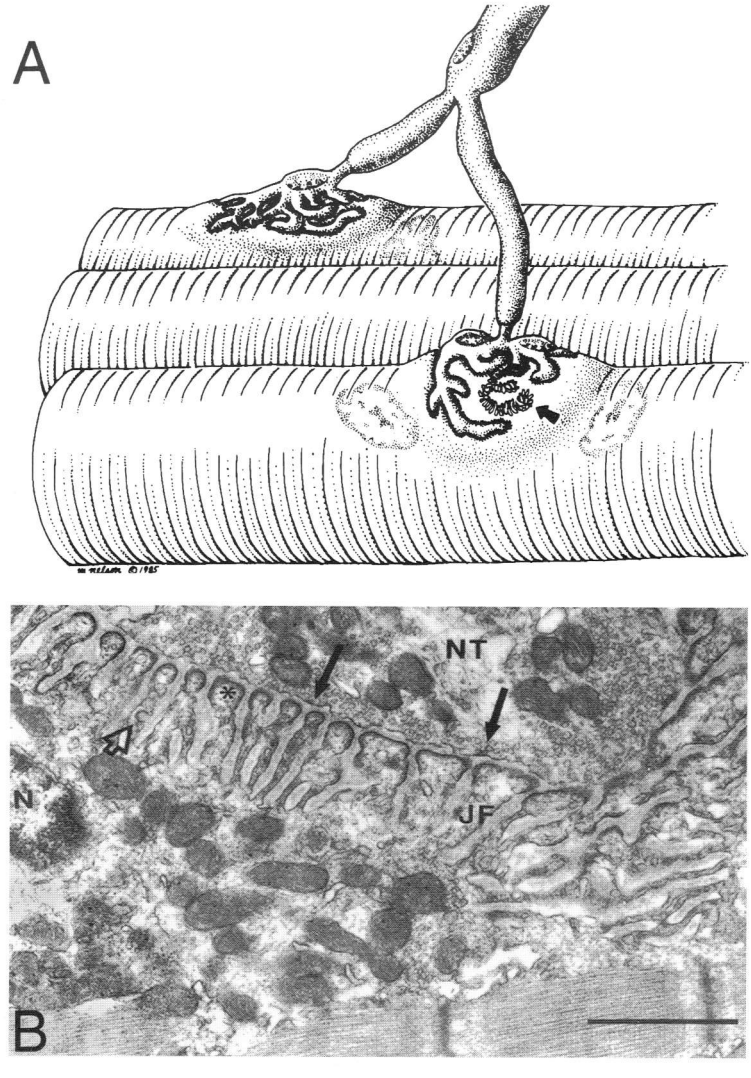

Figure 15.2. Overall organization of mammalian or reptilian NMJ.

(A) Schematic diagram of a branched, myelinated axon innervating two muscle fibers. The myelin sheath ends above the nerve terminals, which are encapsulated by Schwann cells and are twisted to form compact endplates. If the nerve terminal is removed, the openings into JFs are visible (arrow). Schwann cell and postsynaptic sole plate nuclei are also indicated.

(B) TEM view of mouse sternomastoid NMJ. Synaptic vesicles and mitochondria are visible throughout the nerve terminal (NT), and active zones (filled arrows) are localized across from the openings of JFs. Dense postsynaptic membrane is present mostly at the crests of JFs (asterisk), while nondense membrane is mostly lower and sometimes includes fused vesicles (open arrowhead). One sole plate nucleus (N) and numerous mitochondria are visible. Note also the relative regularity of JF contours at the left and center, and the extreme structural complexity at the right (cf. Fig. 15.18A). Scale bar = 1 μm.

From Salpeter (1987), reprinted by permission of Wiley-Liss, Inc., a subsidiary of John Wiley & Sons, Inc.

Salpeter, 1978; Land et al., 1980, 1981, 1984; Salpeter, 1987), which illustrated how quantal packets of ACh would interact with discrete, almost saturated, nonoverlapping areas of postsynaptic receptive surface. The saturated disc model agreed well with contemporary physiological studies that indicated nonoverlapping areas of AChR activation at NMJs with normally active AChE, but suggested the potential for overlap if AChE was inhibited (Hartzell et al., 1975).

Other molecules, such as Na^+ channels, have also been identified at the bottom of JFs (Flucher and Daniels, 1989; Boudier et al., 1992). As the extensive complexity of JFs is incorporated into high-resolution 3-D reconstructions and MCell simulations, the role of JFs and other aspects of neuromuscular function (normal and pathological) are increasingly open to detailed biophysical investigations. Similarly, as the site densities and distributions of the many molecules that participate in central synaptic transmission are defined and incorporated into realistic simulations, complex aspects of synaptic communication and plasticity will become increasingly accessible.

Rationale for Monte Carlo Approach to Simulation of 3-D Diffusion and Chemical Reaction

The simultaneous diffusion of molecules and their chemical reactions in three dimensions can be simulated using one of two fundamentally different methods, based either on finite element (FE) or MC algorithms. Both require significant computer programming and computational resources, and each approximates reality in a different way. The MC approach is more realistic and is generally more expensive computationally, but as 3-D models become more detailed the difference in computer requirements for MC versus FE simulations is not so great as it once was. Prior to the recent explosion in computing power, limited resources dictated that 3-D problems be simplified dramatically, for example by replacing a real in situ synaptic cleft with a flat, isolated, radially symmetrical model. In this way 3-D problems could be reduced to one dimension, and the mathematics of diffusion and chemical reaction could be handled with analytic approximations or sets of ordinary differential equations that could be evaluated with simple finite difference methods. Such *equation-based approaches* disregard the discrete nature of ligand and receptor molecules and instead use hypothetical concentrations that vary smoothly as a function of position and time. The strengths of such simplified approaches are rapid and precise predictions for the average behavior of the model (assuming a small enough time step). However, the drawbacks of simplification may in some circumstances lead to significant errors, and stochastic variability is ignored.

For 3-D FE simulations, the molecular nature of the real system is disregarded, and differential equations are used to compute fluxes and reaction rates between and within spatial subdivisions or voxels (the

finite elements). Concentration gradients are ignored within each voxel (i.e., the contents are assumed to be well mixed), and flow occurs across the interfaces between adjacent voxels (except, of course, where a voxel wall coincides with a diffusion boundary). Thus, as for the simplified one-dimensional (1-D) approach, reactant concentrations vary smoothly throughout space, albeit with small stepwise changes from one voxel to the next. Whereas 1-D approaches subdivide only time, the 3-D FE approach subdivides both time and space, and overly large spatial subdivisions (coarse granularity) can markedly degrade numerical accuracy. Fine granularity is easy to achieve for simple overall spatial configurations (e.g., a cell represented as a subdivided box), and under such conditions this method can be extremely efficient. For complex realistic structures, however, the spatial subdivisions become correspondingly complex to plan and implement, and the number of voxels can grow to be very large. Under such conditions the computational expense increases tremendously, and in no case do FE simulations provide direct information about stochastic variability arising from the spatial configuration and actual finite numbers of participating molecules.

In contrast to the equation-based simulation methods, the MC approach to 3-D diffusion and chemical reaction begins with an arbitrary set of surfaces that represent a subcellular environment (e.g., cell and organelle membranes), and then the surfaces and surrounding space are populated with individual ligand and ligand-binding molecules. With the present version of MCell, the shape of the surfaces can be as realistically complex as desired, as can the biochemical pathways followed by ligand and ligand-binding (effector) sites. Ligand movements approximate Brownian motion by means of random walk displacements, and collisions with surfaces and effector sites can be detected without the use of voxels by tracing random walk trajectories through space with algorithms similar to those used to trace light rays in photorealistic computer graphics. The average radial distance ($\bar{l}_r$) traveled in a random walk step depends on both the specified ligand mobility (diffusion coefficient, D) and the simulation time step (Δt). High numerical accuracy can generally be obtained under conditions in which $\bar{l}_r$ and Δt are orders of magnitude larger than the mean free path and time between collisions, respectively, for true Brownian motion. Another relationship of importance to numerical accuracy is the ratio of Δt to the average lifetimes of the chemical reactant states in the simulation. (Such issues underlying the choice of input parameter values and resulting accuracy are illustrated later in the chapter.)

During each MC time step, Δt, decisions about distance and direction of motion, binding, unbinding, conformational changes, and all other possible events are made by comparing the values of random numbers to MC probabilities that are precalculated for each type of event. The MC probabilities depend on input values for Δt, D, reaction rate constants, and the surface area of effector sites, and they ensure that results for equilibrium or steady-state conditions match analytic expectations

based on bulk solution rate equations. The use of random numbers to make decisions during the simulation is reminiscent of throwing dice, and the term *Monte Carlo* was originally coined in this context by Ulam and Von Neumann during the Manhattan Project (Rubenstein, 1981). Since events occur on a molecule-by-molecule basis, the simulation results include realistic stochastic noise arising from the spatial arrangement and finite number of participating molecules. Averaging over a number, n, of different simulations (run with different random numbers) decreases the noise, but generally only in proportion to $1/\sqrt{n}$. This noise may seem to be a disadvantage of MC simulations, but it is in fact a blessing in disguise because its spectral properties can be compared with the observed properties of noise present in experimental data.

Although the potential realism and generality of MC methods were clear many years ago, large increases in computer speed and memory were required before many applications became feasible. Because of such increases, as well as algorithm optimizations developed for MCell, it is now possible to simulate complex cellular reconstructions on workstations, and very large projects can be ported effectively to massively parallel computer architectures. As mentioned earlier, this level of realism is not simple to implement using FE methods, nor is it clear that an FE approach would be appreciably more efficient. Most importantly, MC simulations can now provide insights into the stochastic variability and nonintuitive behavior of complex 3-D systems containing small numbers of reactant molecules.

MCell Overview

History and Scope

A novel Monte Carlo approach to MEPC simulation was initiated more than a decade ago (see Figs. 21–23 in Salpeter, 1987) in order to advance saturated disc modeling at the NMJ beyond a flat cleft configuration and earlier equation-based simulation methods (Land et al., 1980, 1981, 1984). The new approach led to a computer program that could simulate planar (simplified) JFs (see Fig. 15.13) and was run on an IBM supercomputer (Bartol et al., 1991; Bartol, 1992). A similar program written independently at about the same time focused primarily on delineating and tracking stochastic molecular events that occur during MC simulations of MEPCs (Stiles, 1990) and was initially run on large clusters of VAX superminicomputers. These two programs were merged, and the resulting code again was run on a supercomputer to simulate the effect of AChE site density and hydrolytic rate at the NMJ (Anglister et al., 1994). Other investigators began using the underlying random walk and MC binding-unbinding algorithms (Bartol et al., 1991) to simulate other simplified synaptic systems (Faber et al., 1992; Bennett et al., 1995, 1997, 1998; Wahl et al., 1996; Kruk et al., 1997).

These early MC programs were designed to simulate one type of simplified structure and could not be applied to more realistic problems. Such limits were removed by generalizing and optimizing the MC methods, and the earliest versions of MCell emerged in successive stages (Stiles et al., 1996, 1998). A Model Description Language (MDL) was created to design and control large-scale simulations, as well as to integrate models with 3-D imaging software, and it has evolved into a standardized interface and archiving system.

MCell has been used worldwide at research laboratories since 1997 (see Web sites in note 2), and it now includes new features that dramatically increase its range of application, memory efficiency, and execution speed. For example, many simulations can be run on workstations rather than supercomputers, the realism and speed of the Brownian dynamics random walk algorithms have been greatly enhanced, and the addition of *spatial partitions* renders execution speed essentially independent of the model's geometric complexity. Thus simulations based on large-scale tissue reconstructions can now be run in about the same time previously required for highly simplified structures, in effect reducing the required computer time from many months to hours or even minutes.

Typical events that occur during an MCell simulation include the release of ligand molecules from a structure (e.g., a vesicle), de novo creation or destruction of ligand molecules (e.g., synthesis, hydrolysis, or redox reactions), ligand diffusion within spaces defined by arbitrary surfaces (e.g., pre- and postsynaptic membranes or a cell membrane with attached patch clamp micropipette), and chemical reactions undergone by diffusing ligand and fixed effector (e.g., receptor or enzyme) molecules. Ligands, effectors, reaction mechanisms, 3-D surfaces, and other simulation components are specified using the MDL (Fig. 15.3),[3] a simple programming language that was designed with biologists in mind (Stiles and Bartol, 2000). When a simulation is run, one or more MDL input files are interpreted (parsed) to create the simulation objects, and then execution begins for a specified number of iterations. Each iteration corresponds to one MC time step, Δt, which typically is on the order of 1 μsec for synapses. Simulations can be stopped and subsequently restarted at user-specified *checkpoints* (Fig. 15.3), and when a simulation restarts updated information can be read from the input MDL file(s). Checkpointing is thus a powerful and general way to change run-time parameters such as Δt, reaction rate constants, and surface positions; it can also be used to split long simulations into segments that are run sequentially.

Brownian Dynamics Random Walk

MCell simulates diffusion using a novel Brownian dynamics random walk algorithm that has been highly optimized for speed, numerical accuracy, and use with complex structures. In essence, extensive sets of equally probable radial distances and directions are stored in two look-up

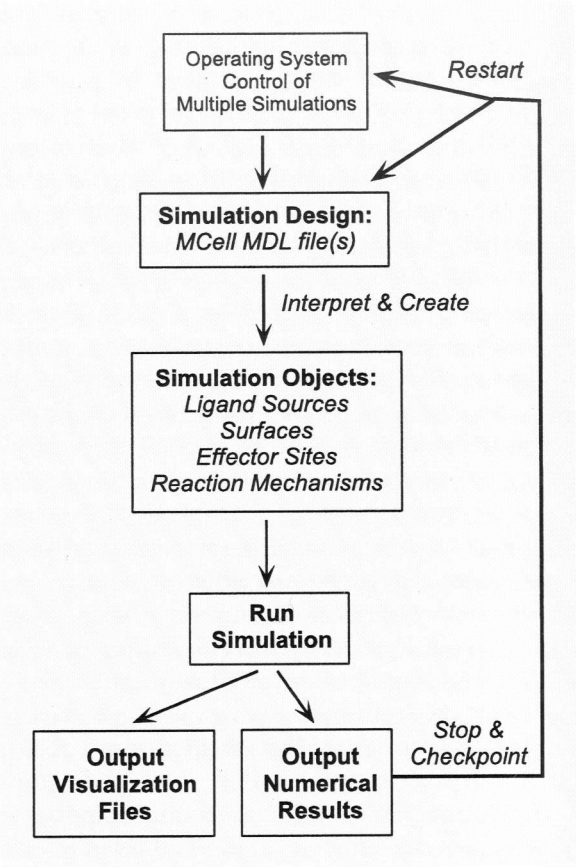

Figure 15.3. Overview of MCell simulation design, execution, and output. Simulations are run in UNIX or Windows environments and are designed using Model Description Language (MDL) text files created by the user or from 3-D surface reconstruction data. When the simulation is initialized, the MDL files are interpreted to create the objects used during execution. Execution continues for a specified number of time steps, and the amount and type of output are under the user's control. Output files fall into three general categories: (1) visualization, used with a variety of 3-D imaging and animation software; (2) numerical results, used to tally the number of reaction intermediates and transitions as a function of time and space; and (3) checkpointing results, used as all or part of the initial conditions for subsequent simulations. In addition, sets of simulations may be controlled using command files that are specific to the computer's operating system (e.g., UNIX shell scripts or DOS batch files).

tables, and one value is chosen from each table to generate each random walk movement. The use of such tables increases execution speed dramatically, and any reduction in accuracy is effectively immeasurable.

The values for the first table are based on diffusion theory and are calculated from a standardized probability distribution function (p_s) for a dimensionless parameter s:

$$p_s = \frac{4}{\sqrt{\pi}} s^2 e^{-s^2}\, ds. \tag{15.1}$$

At the beginning of each simulation, equation (15.1) is integrated numerically to obtain the cumulative probability of s, which then is finely subdivided into bins (generally 1024) of equal area. The mean value of s for each bin is stored in the look-up table, and then, while the simulation runs, values can be chosen from the table as needed using uniformly distributed random numbers. For a ligand molecule with diffusion constant D_L, a chosen value of s is converted to a radial step length (l_r) using a multiplicative scaling factor given by $\sqrt{4D_L(\Delta t)}$, which has units of distance.

For a given value of D_L, the distribution of random walk step lengths changes according to the value specified for Δt. For accurate simulation of diffusion, Δt must be chosen so that the mean radial step length ($\bar{l}_r$) is smaller than the dimensions of restrictive structures in the model. The value of $\bar{l}_r$ is obtained from the expectation value of s and the scaling factor $\sqrt{4D_L(\Delta t)}$ and is given by

$$\bar{l}_r = 2\sqrt{\frac{4D_L(\Delta t)}{\pi}}. \tag{15.2}$$

In order to calculate MC binding probabilities for effector sites located on a surface, it is necessary to know the average random walk displacement with respect to a linear direction oriented perpendicular to the surface ($\bar{l}_\perp$). From a form of equation (15.1) for linear rather than radial displacements,

$$\bar{l}_\perp = \sqrt{\frac{4D_L \Delta t}{\pi}} \tag{15.3}$$

or $\bar{l}_r/2$.

To generate a ligand movement, a randomly chosen radial step length must be paired with an unbiased choice of radial direction. Complete elimination of bias is critical because even a tiny asymmetry can accumulate over thousands of iterations to produce substantial drift. The second look-up table is used to store a set of equally probable radial directions, that is, unit vectors that originate from a point and radiate out in all directions with equal probability. These vectors are calculated numerically when the simulation begins (there are generally more than 130,000), using methods that guarantee the absence of directional bias. Once a value of s and a direction have been chosen for a particular movement,[4] the x, y, and z components of the direction vector are multiplied by the product of s and the scaling factor $\sqrt{4D_L(\Delta t)}$, and the results are added to the present (x, y, z) coordinates of the molecule.

Over any interval of time, Δt, longer than the time between actual Brownian collisions (sub-picosecond scale at room temperature; e.g., Barrow, 1981), a real diffusing molecule follows some tortuous path between a starting position (P1) and an ending position (P2). The molecule's

thermal velocity and the duration of Δt determine the *total* distance traveled, but the *net radial* distance traveled (the length of the vector $\vec{l}_r$ between P1 and P2) is proportional to $\sqrt{\Delta t}$. This proportionality is shown directly for the average distances $\bar{l}_r$ and $\bar{l}_\perp$ in equations (15.2) and (15.3).

In an MCell simulation, the molecule moves along the shorter, straight-line path $\vec{l}_r$ rather than the actual tortuous path, and hence the apparent velocity of motion (1) is less than the true thermal velocity, (2) is not constant for different chosen values of Δt, and (3) decreases as Δt increases. When ligand molecules must diffuse through a restriction (e.g., a vesicle fusion pore) or can bind to effector sites, the apparent velocity of motion directly influences the apparent net flux and also the MC binding probability and hence directly influences numerical accuracy.

Surfaces and Effector Sites

Each curved surface imported into an MCell simulation is actually composed of a polygon mesh (e.g., Figs 15.7, 15.11, 15.16B, and 15.18B), where each mesh element (ME) must be a convex planar polygon. Triangles are used for the most part, because they are guaranteed to be planar (three points in space define a plane) and are required for surfaces that include effector sites. Triangulated meshes are also the typical form of output from 3-D surface reconstruction software.

The MEs within a surface can be individually classified as reflective, transparent, or absorptive with respect to diffusing ligand molecules. Each time that a random walk trajectory (a ray) is generated, it must be traced to see if it intersects with an ME before the endpoint of motion is reached. If so, the final result depends on the properties of the ME at the point of intersection (see Stiles and Bartol, 2000, for a more complete discussion). If the ME contains an effector site at that point and binding occurs, the motion stops and the ligand molecule's fate in subsequent time steps depends on the reaction pathways defined for the effector site. If binding does not occur (whether or not an effector site is present), then (1) if the ME is absorptive, the motion stops and the ligand molecule is removed from the simulation; (2) if the ME is transparent, the intersection is detected and the ray continues through unchanged; or (3) if the ME is reflective, the ray undergoes specular reflection. In the case of (2) or (3), the random walk movement continues until either (a) binding or absorption occurs upon a subsequent intersection or (b) no further reflections occur and the ligand molecule is placed at the end of its remaining trajectory.[5]

Effector sites can be added to one or more MEs of any surface, whether the MEs are reflective, transparent, or absorptive. As illustrated subsequently, effector sites on a reflective surface are typically used to model various types of membrane-bound proteins, while effectors on transparent surfaces generally represent enzyme or other sites localized in an intra- or extracellular scaffold that does not specifically impede lig-

and movement. Effector sites on absorptive surfaces are a special case and could be used to sample the flux across the surface. The kinetic behavior of effector sites is defined by reaction mechanisms specified in an MDL file; it includes not only binding, unbinding, and conformational transitions but also the directionality of binding and unbinding with respect to the surface. For example, simple receptor sites would bind and unbind ligand molecules on only one side of a reflective surface, reuptake sites would bind on the extracellular side and release on the intracellular side, and sites on transparent surfaces would bind and unbind from either side.

To use effector sites in a simulation, a global *effector tile grid density,* denoted here as σ_{EG}, must be specified in units of tiles/μm^2. This parameter determines the maximum density of effector sites that can be added to any surface, so if more than one type of effector is added to the same mesh (e.g., intermixed α-amino-3-hydroxyl-5-methyl-4-isoxazolepropionic acid and *N*-methyl-D-aspartate glutamate receptors), the sum of their densities should not exceed σ_{EG}. To add effector sites to MEs of arbitrary triangular shape, an individual grid is created for each ME, using *barycentric subdivision.* In short this method creates interdigitated triangular effector tiles that cover each ME exactly and have the same triangular aspect ratio as the ME on which they reside (Fig. 15.4). If the ME is large enough to accommodate more than just a few tiles (which is almost always the case), the aspect ratio is unimportant to numerical results. However, long and thin triangles are not optimal for imaging, because effector molecule glyphs placed at the center of mass of each tile (part of MCell's visualization output) appear in unrealistic linear arrays (Fig. 15.4B). With nearly equilateral triangles, on the other hand, the molecule glyphs occupy positions in a seemingly realistic hexagonal array (Fig. 15.4A).[6]

When a simulation begins, MCell makes one pass through each surface that contains effector sites, and for each ME it (1) calculates its area (A_{ME}); (2) performs barycentric subdivision (Fig. 15.4) to obtain an integer number (N_{ET}) of triangular effector *tiles* that cover its surface exactly; (3) calculates the expected number of effector *sites;* (4) calculates the probability (p) that each effector *tile* is occupied by an effector *site* (as opposed to remaining bare surface); and (5) compares the value of a random number, $\kappa(0 \leq \kappa \leq 1)$, with the value of p, to determine the identity of each effector tile.

Chemical Reactions: Monte Carlo Probabilities and Heuristics

Consider a simple reversible reaction between ligand L and effector E:

$$L + E \underset{k_-}{\overset{k_+}{\rightleftharpoons}} LE. \qquad \textbf{(15.4)}$$

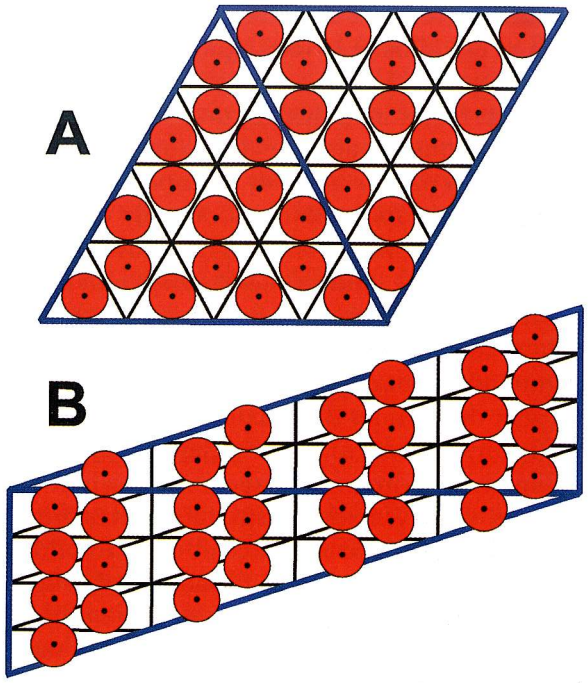

Figure 15.4. Simple examples of barycentric tiling. (A) Two equilateral MEs (heavy blue lines), each with area A_{ME}, subdivided according to the value of A_{ME} and σ_{EG}. In this case a 4×4 barycentric grid is obtained (narrow black lines), producing 16 effector tiles per ME. *(B)* Two nonequilateral MEs, each also with identical area A_{ME}, and therefore also subdivided using a 4×4 barycentric grid. When simulation results are visualized, color-coded glyphs are used to indicate the positions and chemical states of tiles occupied by effector sites. The glyphs typically are shaped and scaled to reflect the molecule being modeled (e.g., AChRs). In this 2-D illustration, red discs are used as glyphs, and every tile is occupied by an effector site. The glyphs are placed at the center of mass of each tile, and with equilateral MEs (*A*) the result is a hexagonal array. With long and thin MEs (*B*) the result is linear arrays. For realistic imaging results, optimized meshes containing nearly equilateral MEs are preferable (cf. Figs 15.13, 15.15, 15.16, and 15.18).

The rate constants k_+ and k_- are phenomenological scaling factors that relate an observed rate of reaction to reactant concentrations in bulk solution (e.g., Hammes, 1978). At a given point in space, the rate equation is

$$-\partial(L) = -\partial(E) = \partial(LE) = [k_+(L)(E) - k_-(LE)]\partial t. \qquad \textbf{(15.5)}$$

Under well-mixed conditions, the concentration terms are independent of space at all times, and the partial differentials can be replaced by finite differences (e.g., $\partial(E)$ and ∂t become ΔE and Δt, respectively). If concentration gradients exist, then equation (15.5) can be simulated using the FE or MC methods discussed earlier. With the FE approach, equation (15.5) would be used in finite difference form within each voxel, and flux J between each voxel would be calculated with a 1-D finite dif-

ference simplification of the diffusion equation $J = -D_L \nabla(C_L)$, where C_L is ligand concentration. With the MC approach, net random walk motion determines ligand flux directly, and (as outlined below) the rate constants k_+ and k_- must be converted into dimensionless probabilities p_b and p_k, respectively.

If the binding step in equation (15.4) is taken in isolation, then equation (15.5) becomes

$$-\partial(L) = -\partial(E) = \partial(LE) = k_+(L)(E)\partial t, \tag{15.6}$$

and the number of binding events ($N_B = \Delta(LE)$) expected per unit effector concentration (E), in bulk solution during time Δt, is given by $(k_+)(L)(\Delta t)$. The value of p_b for an effector site E is calculated from the ratio N_B/N_H, where N_H is the average number of times during Δt that ligand molecules "hit" (i.e., random walk trajectories intersect) the effector tile on which site E is located. (This use of N_B and N_H is a useful conceptual simplification; for a full derivation of p_b, N_H, and p_k, see Stiles and Bartol [2000].) The value of N_H depends on A_{ET}, the area of the tile, and since A_{ET} generally differs for each ME($A_{ET} = A_{ME}/N_{ET}$), N_H and therefore p_b also differ for each ME. As shown in Fig. 15.5, N_H can be derived conceptually by first defining a direction vector ψ that is perpendicular to the ME. The average net distance traveled by ligand molecules along ψ is given by $\bar{l}_\perp$ (equation (15.3)). On average, half of the molecules within this distance will step away from the ME, while the other half will step toward it (and therefore will hit it). For an effector E in particular, $2N_H$ ligand molecules thus are contained within a volume V_{ET} that extends both "above" and "below" the tile for a distance $(\pm)\ \bar{l}_\perp$ along ψ. The value of V_{ET} therefore is $2(\bar{l}_\perp)(A_{ET})$ and N_H is given by $(\bar{L})(N_a)(V_{ET})/2$, where N_a is Avogadro's number. A final expression for p_b is

$$p_b = \frac{(f_s)(f_A)(k_+)(\sigma_{EG})}{2(N_a)} \left(\frac{\pi(\Delta t)}{D_L}\right)^{1/2}, \tag{15.7}$$

where σ_{EG} is the effector tile grid density. The factor f_A (≥ 1) is given by the ratio of two areas, A_{ET} and $1/\sigma_{EG}$, i.e., $f_A = 1/(A_{ET}\sigma_{EG})$. The additional term ($f_s$) is unity if ligand molecules bind to either side of the ME (e.g., the transparent surfaces as illustrated in Fig. 15.7). For a reflective surface with binding allowed from only one side, V_{ET} would extend a distance $\bar{l}_\perp$ either "above" or "below" the ME and therefore would be halved. As a result N_H would also be halved, and $f_s = 2$ would be used in equation (15.7) to double the value of p_b.

Whenever a diffusing ligand molecule hits an effector site on an ME, the occurrence of binding is tested by comparing the value of a random number ($0 \leq \kappa \leq 1$) to the value of p_b for the ME. Because the apparent MC velocity of motion decreases if Δt is increased, p_b must increase to keep the average MC binding rate equal to the bulk solution binding rate. Equation (15.7) shows that p_b scales with $\sqrt{\Delta t}$ (because $\bar{l}_\perp$ scales with $\sqrt{\Delta t}$; equation (15.3)), so if the simulation time step is doubled and all

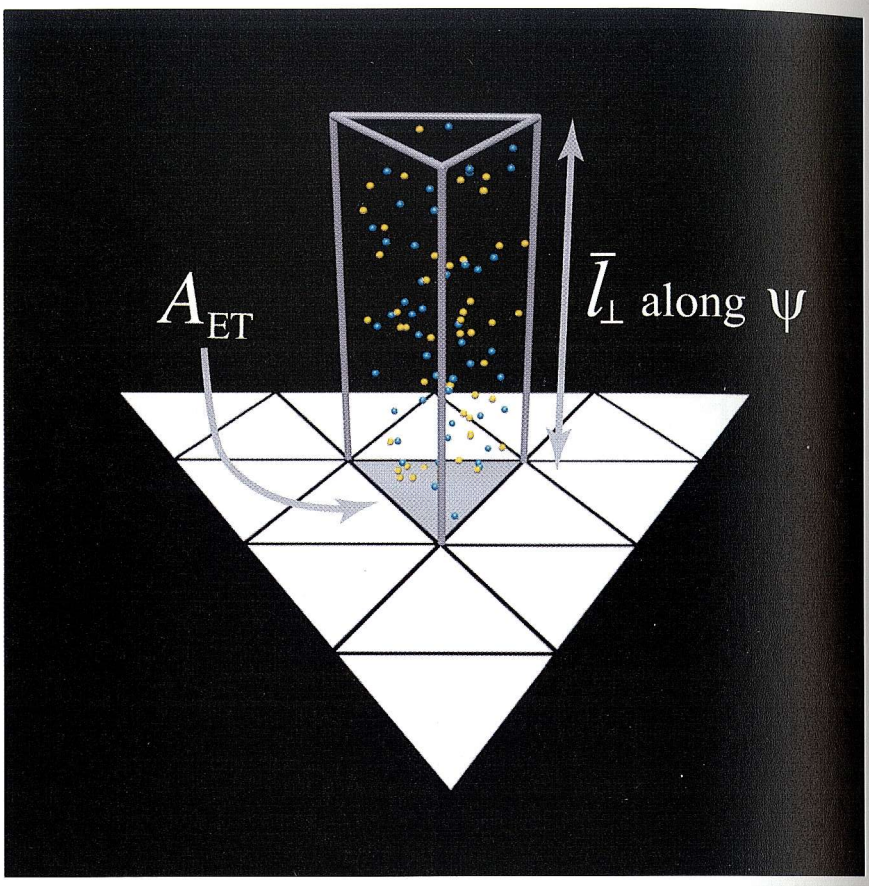

Figure 15.5. Derivation of N_H. The illustrative ME shown here is subdivided into 16 effector tiles, one of which is an effector site E (gray). During a time step, Δt, diffusing ligand molecules moving in random directions are displaced an average distance $\bar{l}_\perp$ along a direction ψ perpendicular to the ME. On average, half of the molecules (e.g., blue spheres) move away from the ME and half (e.g., yellow spheres) move toward it, so the value of N_H is one-half the number of molecules contained within the volume $V_{ET} = 2(\bar{l}_\perp)(A_{ET})$ indicated by the extruded gray prism for the portion of V_{ET} above the ME. Of course some of the yellow molecules actually move outside V_{ET} during Δt (and hence do not hit E), but on average they are replaced by an equal number of molecules moving into V_{ET} from the surrounding space.

other input parameters are held constant, the value of p_b increases by $\sqrt{2}$. The resulting impact on numerical accuracy depends on the new value of p_b and other factors. It is necessary that the value of p_b not exceed unity.

If the unbinding step in equation (15.4) is taken in isolation, the transition is a unimolecular Poisson process, and equation (15.5) becomes

$$d(L) = d(E) = -d(LE) = k_{-}(LE)\ dt. \tag{15.8}$$

Other types of unimolecular transitions in MCell simulations include effector site isomerizations and ligand production, transformation, and destruction (Fig. 15.6). In any case, the generic first-order rate constant k has the units of inverse time, and the lifetime of the source state is exponentially distributed with a mean value (τ) of $1/k$. The MC probability (p_k) is the likelihood that the transition occurs during time Δt and is given by $1 - \exp(-k\Delta t)$. If the source state has a choice of n unimolecular transitions with rate constants $k_1, \ldots, k_n$ (e.g., the double-bound A_2R state in Fig. 15.6C has two unbinding paths and one isomerization path), τ is given by $1/\Sigma^n k$, the total probability (p_T) of any transition is

$$p_T = 1 - \exp\left[-\left(\sum^n k\right)\cdot \Delta t\right], \tag{15.9}$$

and the probability of the pathway with rate k_i is

$$p_i = p_T \cdot \frac{k_i}{\sum^n k}. \tag{15.10}$$

The decision between all possible events (including no transition) is made by comparing a single random number ($0 \le \kappa \le 1$) to the cumulative set of probabilities (p_1, $p_1 + p_2$, . . . , Σp, 1).

When an irreversible reaction is simulated using MC methods, the algorithm design and use of p_b and p_k are straightforward because each ligand and effector molecule can undergo a maximum of only one transition per time step. When reversible reactions are simulated, however, the algorithm design can take different forms. In a "first-order" approach, each molecule remains limited to a maximum of one transition per time step. "Higher-order" approaches allow individual molecules to undergo multiple "sub-Δt" transitions and thus allow some degree of "hidden" reversibility during each iteration. Using the reaction of equation (15.4) as a simple example, a particular effector site initially in the LE state might unbind at some point during the time step, and then sometime later during the same time step it could become bound again.

If a higher-order approach can be suitably balanced for complex cyclic reactions (e.g., Fig. 15.6B), its advantage is improved numerical accuracy for a given value of Δt. Testing different higher-order approaches involves simulating a set of simple and complex reactions at equilibrium and comparing the fractional amounts of each reactant to analytic predictions or to a finite difference simulation of the corresponding rate equations. MCell uses an extensive set of optimized rules that govern sub-Δt transitions, and the numerical accuracy for both simple and highly complex reactions is illustrated briefly in the following section.

Chemical Reactions: Numerical Accuracy

The use of equilibrium conditions to quantify the accuracy of MCell simulations is summarized in Tables 15.1 and 15.2, and Figs. 15.7 and 15.8.

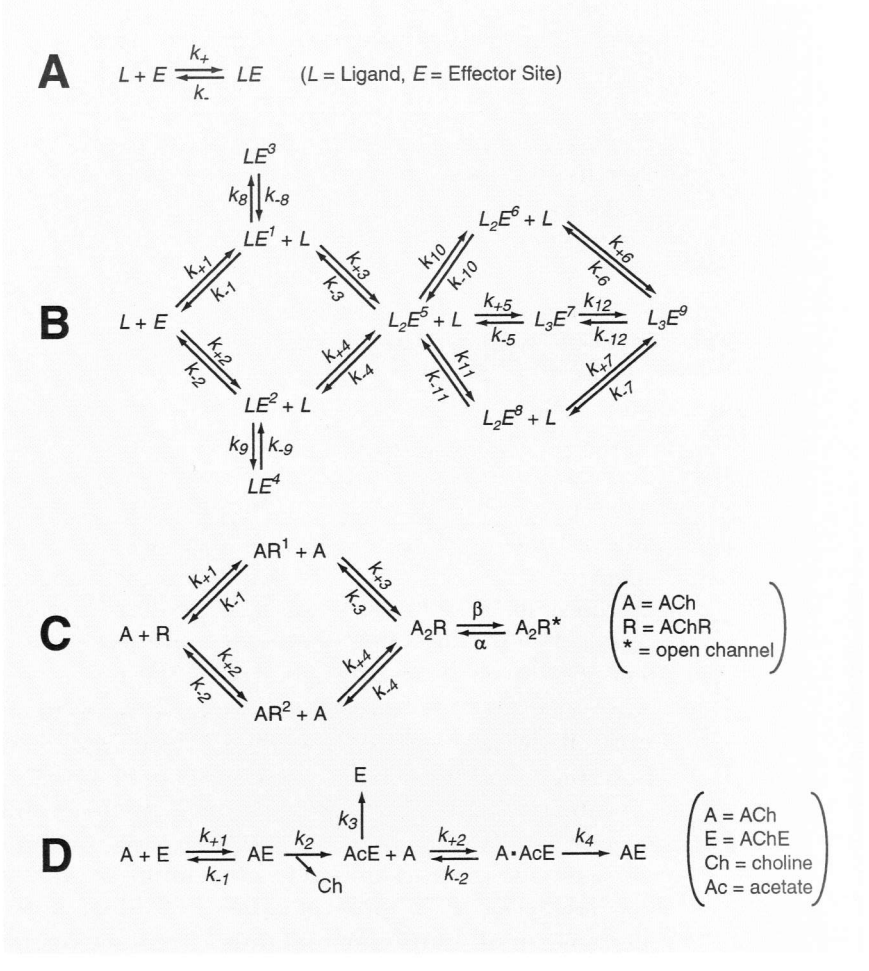

Figure 15.6. Examples of chemical reaction mechanisms used with MCell simulations. Rate constants for bimolecular associations (k_{+n}) are given in units of $M^{-1}sec^{-1}$, and for unimolecular transitions (k_{-n} or k_n) in units of sec^{-1}. Ligand diffusion constants are given as cm^2/sec.

(A) Simple reversible binding reaction, as used for the equilibrium simulations of Table 15.1 and the relaxation simulations of Fig. 15.8. Except as indicated otherwise in Table 15.1, the values of k_+ and k_- were 2×10^8 and 50,000, respectively. D_L was 2×10^{-6}.

(B) Complex reaction mechanism for an effector with three ligand-binding sites and 10 possible states (indicated by superscripts). This mechanism, with both parallel and sequential binding, unbinding, and isomerization transitions, was designed specifically to test MCell's rules governing sub-Δt transitions (see text). Numerical accuracy for this mechanism is illustrated in Table 15.2. D_L was 2×10^{-6}, and rate constant values were as follows: k_{+1}, 1×10^8; k_{-1}, 10,000; k_{+2}, 1.5×10^8; k_{-2}, 10,000; k_{+3}, 5×10^7; k_{-3}, 7000; k_{+4}, 7.5×10^7; k_{-4}, 7000; k_{+5}, 8.5×10^7; k_{-5}, 15,000; k_{+6}, 1×10^7; k_{-6}, 50,000; k_{+7}, 2×10^7; k_{-7}, 50,000; k_8, 20,000; k_{-8}, 35,000; k_9, 25,000; k_{-9}, 33,000; k_{10}, 40,000; k_{-10}, 45,000; k_{11}, 38,000; k_{-11}, 38,000; k_{12}, 50,000; k_{-12}, 2000.

(C) Mechanism used for AChR activation in MEPC simulations. D_{ACh}, 2.1×10^{-6}; k_{+1}, k_{+2}, k_{+3}, k_{+4}, 1.35×10^8; k_{-1}, k_{-2}, k_{-3}, k_{-4}, 64,286; β, 48750; α, 1250.

Effector sites were dispersed uniformly throughout space within a reflective spherical shell, on a series of inner concentric shells made of transparent polygons (Fig. 15.7). A reaction mechanism was chosen (e.g., Fig. 15.6A or 15.6B),[7] and the effector sites were initialized either to the unbound state or to an expected equilibrium distribution (to simulate either the approach to or maintenance of equilibrium, respectively). MCell's checkpointing feature was used to introduce ligand molecules at uniform concentration throughout the shell. Checkpointing was also used to create an instantaneous change in free ligand concentration during a simulation,[8] so that the relaxation to new equilibrium conditions could be quantified (Fig. 15.8).

Table 15.1 shows how simulation results for a simple reversible binding reaction (equation (15.4) and Fig. 15.6A) changed as a function of the MC time step, Δt. With all other input parameters held constant, a decrease in Δt (1) decreases the length of random walk movements; (2) decreases the values of the MC binding and unbinding probabilities, p_b and p_k; and (3) decreases the simulation's temporal granularity with respect to the theoretical average lifetimes of reaction intermediates (average lifetimes are constant at equilibrium and are shown in Table 15.1). Because the reaction space in this example is symmetrical, the scaling effect of Δt on random walk movements is unimportant, and the simulation accuracy can be assessed in terms of temporal granularity and MC probability values. When Δt is small (i.e., when the temporal granularity is fine and p_b and p_k are both much less than unity), the relative error in the simulation results (average fractional concentration of each intermediate) is far below 1%. If an inappropriately large value of Δt is chosen so that p_b exceeds unity (equation (15.7)), the results reflect the nonsensical value of p_b and will show an excess of unbound ligand and effector molecules.

Values of p_b that approach, but do not exceed, unity are perhaps surprisingly well tolerated, as long as the increase in Δt does not also degrade the temporal granularity by a large amount. This last point is clearly shown by another set of results in Table 15.1, obtained from simulations in which the effector sites were all placed on the inside of the outer shell, rather than on the inner concentric shells. Under these conditions, identical equilibrium results are expected because the same amounts of ligand and effector sites are present in the same total reaction volume.

Figure 15.6. (opposite) continued

(D) Mechanism for ACh hydrolysis by AChE in MEPC simulations. This reaction illustrates unimolecular transitions in which ligand molecules are produced (choline, Ch), transformed (ACh to acetate, Ac), or destroyed (Ac). It also includes ACh binding to the acetylated AChE intermediate (AcE) to simulate excess substrate inhibition (Rosenberry, 1979). The effective turnover number for ACh hydrolysis was 16,000/sec (Stiles, 1990). k_{+1}, 2×10^8; k_{-1}, 14,000; k_2, 112,000; k_3, 18,667; k_{+2}, 5×10^6; k_{-2}, 21,429; k_4, 1867.

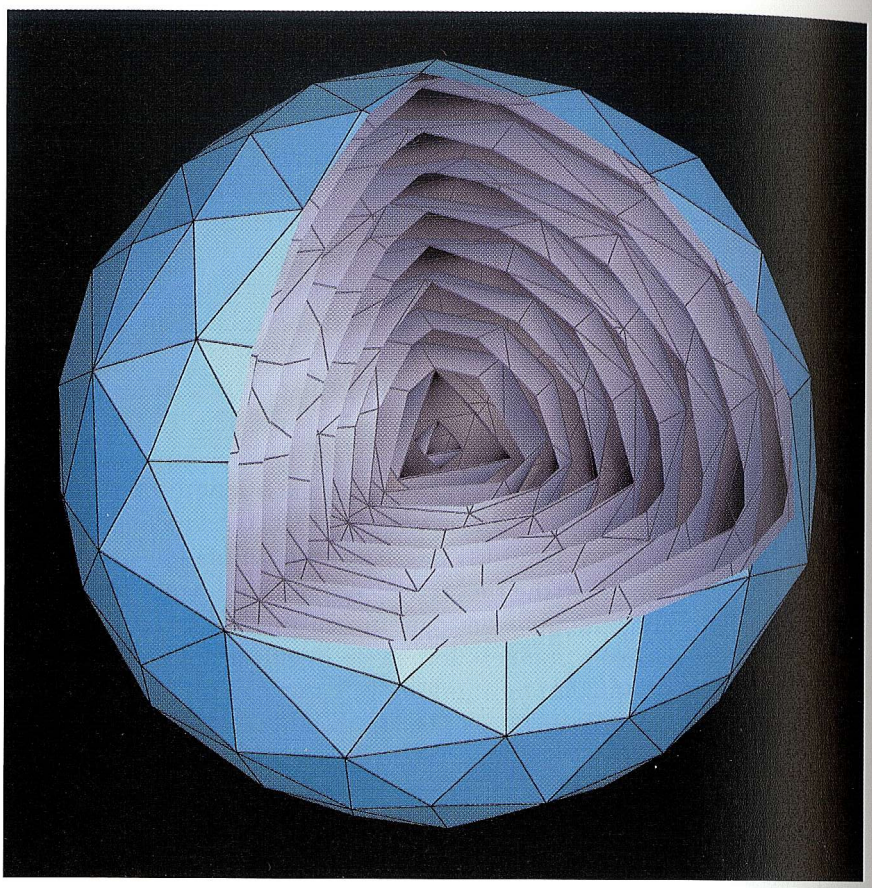

Figure 15.7. Cutaway view of radially symmetrical reaction volume used for equilibrium simulations. The outer shell (light blue mesh, actual volume 0.0628 μm^3, effective radius 0.247 μm) is reflective to diffusing ligand molecules, while the 10 inner shells (gray) are transparent. Effector sites (not shown) were distributed either on the inner shells to simulate a well-mixed solution (nearest-neighbor distance was the same within a shell as between adjacent shells) or on the inside surface of the outer shell (see text and Table 15.1).

However, in this case the ligand molecules bind to a reflective (rather than transparent) surface, and this doubles the value of p_b for a given value of Δt (Table 15.1, and see discussion of the factor f_s in equation (15.7)). Comparison of these results (circa 2.5% error obtained with $\Delta t = 3$ μsec and $p_b = 0.72$) to the earlier results obtained with (1) the same time step and smaller binding probability (circa 2.5% error, $p_b = 0.36$) or (2) a longer time step but similar binding probability (6–13% error, $\Delta t = 10$ μsec and $p_b = 0.66$) shows clearly that simulation accuracy can be more sensitive to temporal granularity than to binding probability.

As shown in Table 15.2, equilibrium simulations of extremely complex reactions (Fig. 15.6B) also yield relative errors much less than 1%,

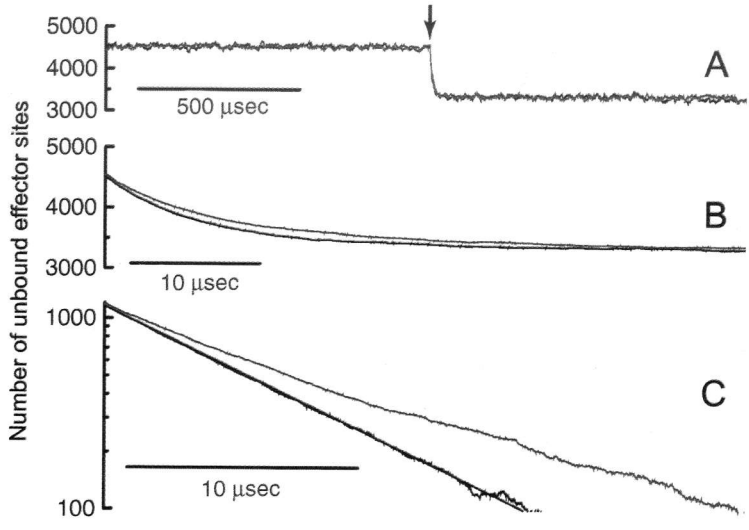

Figure 15.8. Example of equilibrium relaxation simulations for the reaction mechanism of Fig. 15.6A. Effector sites were present either on the inner shells shown in Fig. 15.7 (black data points) or on the inside surface of the outer shell (red data points).

(A) The initial equilibrium conditions were perturbed by doubling the number of free ligand molecules at the time indicated by the arrow; hence the number of unbound effector sites (ordinate values) relaxes to a new, lower equilibrium value. Results are shown for individual simulations (Δt = 0.1 μsec).

(B) The relaxation transition shown on an expanded time scale, with results averaged across five simulations for each distribution of effector sites.

(C) A semilog plot of the averaged relaxation transition (final average equilibrium number of unbound effector sites subtracted from ordinate values). With effector sites distributed on the inner shells, the transition is first order (linear fit superimposed on black data points). With effector sites on the outer shell (red data points), the curved transition reflects higher-order kinetics that include ligand diffusion time.

given reasonably small values of Δt. Thus simulation accuracy is largely independent of reaction complexity, and this independence arises largely from the optimized implementation of sub-Δt binding and unbinding transitions discussed earlier. Figure 15.8 shows results from equilibrium relaxation simulations for the simple reaction of Fig. 15.6A, obtained with effector sites located either on the concentric shells or on the outer shell alone. In the former case, the reaction space simulates a well-mixed solution, and hence the relaxation follows an expected exponential time course. With effectors on the outer shell (circa 0.25 μm radius), however, the diffusion time from the center of the sphere to the periphery becomes a component of the relaxation, which therefore displays complex higher-order kinetics. This result underscores the importance of accurate 3-D simulations for problems such as second messenger diffusion and signaling in subcellular locales.

Table 15.1. Numerical Accuracy for a Simple Reversible Binding Reaction

			Percentage error		
Δt(μsec)	p_b	p_k	L(τ = 42 μsec)	E(τ = 28 μsec)	LE(τ = 20 μsec)
			Effector sites on concentric shells		
0.01	0.021	0.00050	+0.10	+0.15	−0.21
0.10	0.066	0.0050	+0.13	+0.20	−0.49
1.00	0.21	0.49	−0.39	−0.59	+0.82
3.00	0.36	0.14	−1.7	−2.6	+3.6
10.0	0.66	0.39	−6.3	−9.4	+13
10.0*	1.32	0.39	+5.7	+4.3	−6.0
			Effector sites on outer shell		
3.00	0.72	0.14	−1.6	−2.4	+3.4

Note: The reaction mechanism and rate constants are given in Fig. 15.6A, and simulations were run using the radially symmetrical structure shown in Fig. 15.7. For each set of conditions, 20 simulations were started at equilibrium and run for 20,000 iterations with a total of 7750 effector sites. The total number of ligand molecules was 10,000, except in one case (*) where k_+ was doubled and the amount of ligand was reduced to keep the expected mean number of bound (LE_{eq}) and unbound (E_{eq}) effector sites constant. LE_{eq}, E_{eq}, and L_{eq} (expected mean for unbound ligand molecules) were calculated from analytic equilibrium expressions, as were the expected mean lifetimes (τ) for each intermediate. During a run, the number of molecules in each state fluctuates around some average value (see Fig. 15.8A), which was calculated after the run had been completed. These values then were averaged across the set of 20 simulations to obtain grand averages for the MC results (L_{MC}, E_{MC}, and LE_{MC}). To calculate the percent error values shown in the table, the MC grand averages were compared with the analytically predicted means, e.g., $(E_{MC}/E_{eq} - 1) \times 100$ for unbound effector sites. With small values of Δt and correspondingly small values of p_b and p_k, the MC results are fully converged. As Δt, p_b, and p_k increase, the accuracy is reduced, with an excess of the bound state (LE) as long as p_b remains less than unity. If p_b exceeds unity (*), then there can never be enough binding events per unit time, and the direction of error reverses. The temporal granularity (value of Δt relative to the values of τ) is another important factor underlying accuracy, as can be seen by comparing the results obtained with effector sites on the outer shell to the results obtained with effectors on the inner concentric shells (see text).

Simulation of Acetylcholine Exocytosis

The earliest models of MEPC generation simplified NMJ architecture to a flat, coin-shaped diffusion space and used either an analog computer (Rosenberry, 1979) or differential equation–based simulation methods (Wathey et al., 1979; Land et al., 1980, 1981, 1984; Pennefather and Quastel, 1981; Madsen et al., 1984). Synaptic ACh appeared instantaneously as either a point source or another simple distribution centered within the space. With the introduction of early MC algorithms, planar

Table 15.2. Numerical Accuracy for a Complex Cyclic Reaction

	L	E	LE	LE^2	LE^3	LE^4
τ (μsec)	232	32.5	27.7	22.6	28.6	30.3
Percentage error	−0.25	−0.63	+0.021	−0.28	+0.34	−0.32
	L_2E^5	L_2E^6	L_2E^8	L_3E^7	L_3E^9	
τ (μsec)	9.76	21.6	24.7	15.4	9.80	
Percentage error	+0.12	+0.22	+0.28	+0.063	+0.0079	

Note: The reaction mechanism and rate constants are given in Fig. 15.6B, and otherwise the simulations were run and results were analyzed as described in the note to Table 15.1. A single example is shown for fully converged conditions with effector sites on the concentric shells (Δt = 0.1 μsec).

JFs were added to a model NMJ (Bartol et al., 1991), and the impact of AChE site density and hydrolytic rate was investigated (Anglister et al., 1994). More recently early versions of MCell have been used to add a simplified vesicle and fusion pore to simulations of ACh exocytosis and MEPC generation (Stiles et al., 1996, 1998), and they have also been used for detailed modeling of MEPC temperature sensitivity (Stiles et al., 1999). In all of these studies, the model results and predictions were tested against *average* values of experimental measurements (e.g., amplitude, rise time, and fall time), and therefore the simplified models were adequate. However, more realistic models are required to investigate *distributions* of measured values (i.e., synaptic variability and plasticity).

The first step in developing more realistic models is to replace flat surfaces with membrane contours. In general this requires high-resolution 3-D reconstructions and polygon meshes that are optimized for use in simulations. To introduce key concepts and methods, in this section we illustrate the use of a complex polygon mesh to represent a synaptic vesicle that merges smoothly with an expanding exocytotic fusion pore. The diffusion of ACh into a synaptic cleft is simulated, and the predicted time course is shown to match earlier results that had been tested carefully to ensure high accuracy (Stiles et al., 1996, 1998). These earlier results were obtained with a much simpler shape for the vesicle and pore, so the agreement with the present findings both confirms the earlier conclusions and validates the accuracy of the new simulations. We show that the choice of $\bar{l}_r$ (and therefore Δt) is particularly important to numerical accuracy when ligand molecules diffuse through a constriction like the fusion pore, and we also briefly discuss the use of an optimization (spatial partitioning) that renders execution speed nearly independent of mesh size and complexity.

Figure 15.9 shows a same-scale comparison of the polygon mesh vesicle-pore model and the earlier simplified configuration (cube with cylindrical pore composed of rectangular facets). The cube and sphere have the same volume (2.7×10^4 nm^3) and represent the lumen of a

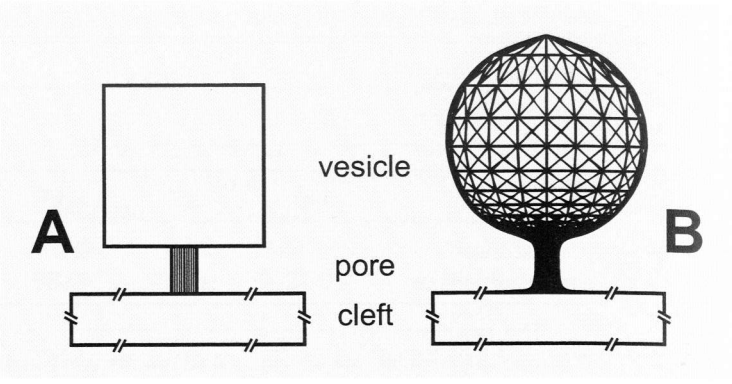

Figure 15.9. Simplified and realistic models of a synaptic vesicle and exocytotic fusion pore.

(A) Simplified, cube-shaped vesicle (30 nm side length) that communicates with the synaptic cleft through a cylindrical pore composed of 16 rectangular facets.

(B) Polygon mesh model of vesicle and pore, composed of 1580 triangles. See text for discussion of vesicle volume and pore dimensions.

synaptic vesicle at the NMJ, with actual (sphere) or equivalent (cube) radius of 18.6 nm. The pore height (h) is 9 nm in both cases (i.e., midway between a single and double thickness of plasma membrane). The average radius (r) of the mesh pore is matched to the exact radius of the cylindrical pore (2.5 nm in this illustration). Simulations were run either with a fixed value of r as shown or with r increasing at a constant rate of 25 nm/msec to simulate fusion pore expansion at the NMJ (Stiles et al., 1996).

For this model of ACh exocytosis, the steepest concentration gradient is across the pore height h. Therefore the rate of ACh efflux is mostly determined by the pore geometry, that is, its "resistance." Concentration gradients do form inside the vesicle and cleft as well, but their significance depends on the value of r. At very small r, the concentration drop across h is very steep (the pore "resistance" is very high) and almost completely limits ACh efflux. For larger values of r, the vesicle and cleft gradients become increasingly significant, but they are appreciably steep only within a distance several times r from the inner and outer pore openings (Stiles et al., 1996). The consequences are that (1) the bounding shape of the vesicle should not affect ACh efflux significantly, although the vesicle volume is an important factor (thus simulation results obtained with the polygon mesh model should match results obtained with the simplified vesicle and pore), and (2) for accurate simulation of ACh efflux, the random walk algorithm must correctly produce concentration gradients over distances comparable to r.

Because the MCell random walk algorithm is grid-free and selects from an extensive set of radial distances and directions for each movement, concentration gradients are simulated accurately within distances

nearly as small as the average step length $\bar{l}_r$. Thus, for accurate simulation of ACh exocytosis, the time step Δt need only be chosen so that $\bar{l}_r$ (equation (15.2)) is somewhat smaller than r.[9] However, if the value specified for Δt is too long and $\bar{l}_r$ is appreciably larger than r, then the concentration gradients inside the vesicle, pore, and cleft will not be steep enough. As illustrated subsequently, the apparent rate of ACh efflux can then easily be slowed by an order of magnitude.

Each simulation of ACh efflux was begun using checkpointing to ensure uniform initial ACh concentration within the vesicle.[10] Figure 15.10 (inset) shows four examples of ACh efflux curves that were obtained using the simplified vesicle structure and fixed r (Fig. 15.9A) and illustrates the dramatically slowed emptying that occurs with increasing Δt. Each of these curves has the form of an exponential decay (Stiles et al., 1996, 1998), and the main panel of Fig. 15.10 shows the e-fold emptying time (τ) plotted as a function of the ratio $\bar{l}_r/(\bar{l}_r + r)$. Essentially identical

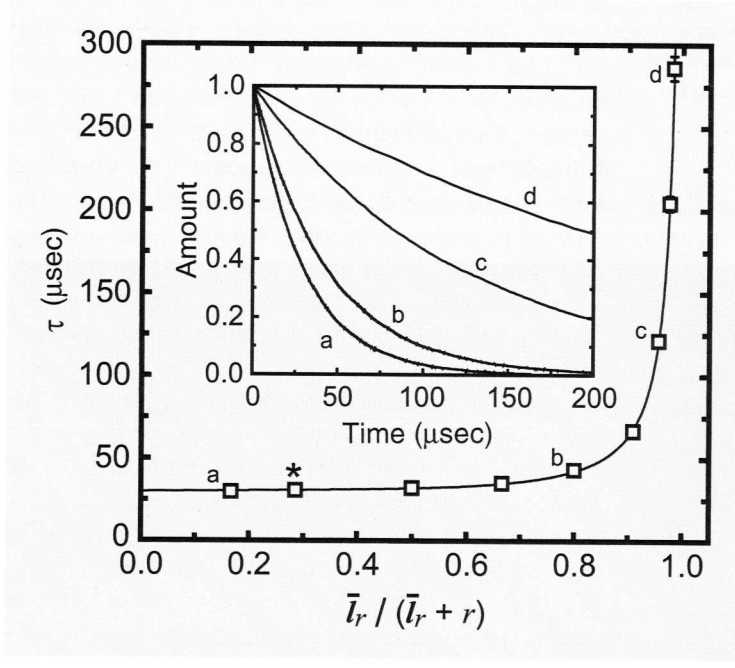

Figure 15.10. Simulation of ACh exocytosis through a fusion pore with constant radius (r = 2.5 nm, Fig. 15.9A). Inset shows the time course of vesicle emptying obtained with Δt values of approximately 82 psec, 33 nsec, 1.0 μsec, and 7.3 μsec for curves a–d, respectively ($D_{ACh} = 6 \times 10^{-6}$ cm^2/sec). Ordinate values are normalized to the starting amount of ACh, and each curve is the averaged result of 10 simulations. Such exponential emptying curves were fitted to obtain e-fold times, and the resulting values of τ were plotted (open squares in main panel, mean ± SD for 10 simulations) as a function of the ratio $\bar{l}_r/(\bar{l}_r + r)$. As indicated by the fitted curve, τ converges to the correct value when $\bar{l}_r$ is less than r. The point marked with an asterisk was obtained with $\bar{l}_r = 0.4r$, and this condition was used for simulations of exocytosis through an expanding pore (Figs. 15.11 and 15.12).

results are obtained with the polygon mesh structure (not shown, but see subsequently), so r in this ratio is either the average (polygon mesh) or exact (simple model) pore radius. As the value of $\bar{l}_r/(\bar{l}_r + r)$ decreases (i.e., as $\bar{l}_r$ becomes small compared with r), the value of τ converges to circa 30 μsec. For the case with the longest time step (i.e., with $\bar{l}_r$ much greater than r), the apparent value of τ (circa 300 μsec) is almost an order of magnitude larger than the correct value, because the ACh concentration gradients do not form properly in the pore and immediate vicinity.

To illustrate and validate simulation of ACh exocytosis through a realistic expanding fusion pore, the polygon mesh structure was interpolated (morphed) 200 times, between limiting average radii of 0.93 nm and 5.0 nm (Fig. 15.11). This starting radius simulates instantaneous initial opening to a conductance of circa 300 pS, that is, gap junction dimensions. The ending radius corresponds to an omega figure at the NMJ and is reached by the time the vesicle empties if the pore expands at 25 nm/msec after the initial opening (see Stiles et al., 1996, for additional details). The sequence of morphed structures then was used in a series of checkpointed simulations, in which the elapsed time for each checkpoint (dictated by the expansion rate and number of morphs) was circa 0.8 μsec. For each run in the sequence, Δt was chosen so that $\bar{l}_r$ remained about 40% of r. This maintained high numerical accuracy throughout the sequence (see equivalent value of $\bar{l}_r/(\bar{l}_r + r)$ marked by an asterisk in

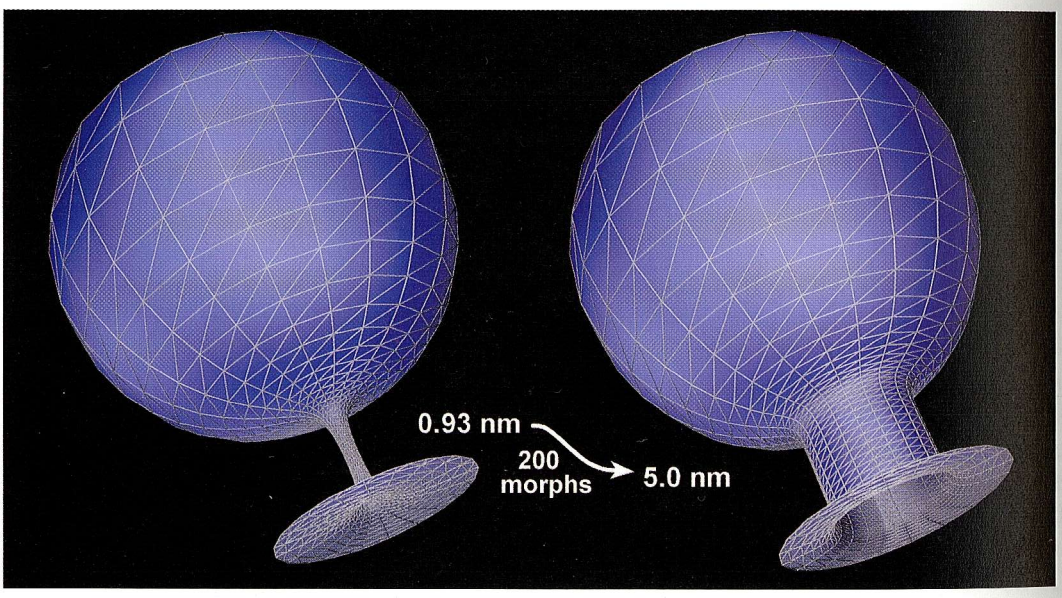

Figure 15.11. Realistic expanding exocytotic fusion pore. The structures for the beginning and ending average pore radii (0.93 and 5.0 nm, respectively) are shown. Using 3-D solid modeling software, smoothly interpolated structures (morphs) were created, so that a total of 200 could be used in a sequence of MCell checkpoints.

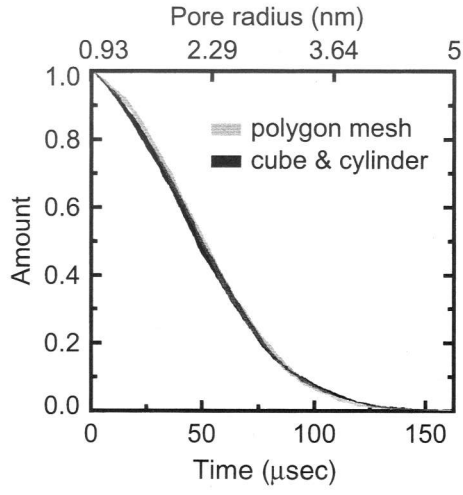

Figure 15.12. Simulation of ACh exocytosis through an expanding fusion pore. The time course of vesicle emptying is shown for the realistic (polygon mesh) and simplified (cube and faceted cylinder) models of a fusion pore expanding at 25 nm/msec ($D_{ACh} = 6 \times 10^{-6}$ cm^2/sec). The thickness of each curve represents the 95% confidence interval obtained from five simulations for each structure. Ordinate values normalized as for Fig. 15.10 (inset).

Fig. 15.10). The value of Δt therefore increased from about 45 psec for the first run, to about 1.3 nsec for the last run (D_{ACh} was 6×10^{-6} cm^2/sec).

Figure 15.12 shows the sigmoidal ACh efflux curve obtained with the expanding fusion pore, and for comparison it also shows the analogous curve obtained when r was increased at the same rate for the simplified structure. The two curves are essentially indistinguishable and therefore validate the accuracy of MCell's diffusion algorithms used with complex polygon meshes. As previously reported (Stiles et al., 1996), the vesicle empties within about 150 μsec, at which time r reaches about 5 nm. In addition the vesicle content is reduced to about 20% of the starting amount within about 80 μsec, a length of time comparable to the 20–80% rise time of MEPCs at room temperature (Stiles et al., 1996, 1999).

Each time that a diffusing ACh molecule takes a random walk step on its way out of the vesicle, its trajectory must be traced to find the nearest intersection with a polygon (if any). This search for intersections is one of the most time-consuming steps in an MCell simulation, and, unless the search algorithm is optimized using spatial partitions, computation time scales with the number of polygons that compose the surface(s) in the simulation. Spatial partitions are simply transparent planes (ligands pass through unhindered) that can be placed in arbitrary positions along the x, y, and/or z axes to subdivide the simulation space into smaller compartments (see Stiles and Bartol, 2000, for further details). When the simulation begins, the polygons contained (wholly or partly) within each compartment are identified. As the simulation runs, random walk trajectories that originate in a certain compartment need only be traced for

intersections with those polygons in the same compartment. If no intersections occur and the trajectory projects into the next compartment, the process continues as required. If each compartment contains only a small number (n_c) of polygons and the total number of polygons in the simulation is N_s, then the optimal increase in execution speed is of order N_s/n_c, with no loss of numerical accuracy.

For example, the vesicle-pore mesh shown previously in Figs. 15.9 and 15.11 contains 1580 polygons, and if an exocytosis simulation is run without spatial partitions the computer time increases by a factor of nearly 300. Thus a simulation that ordinarily requires 1 min with partitions would require 4.5 h without partitions, and a set of checkpoint simulations that ordinarily runs in 1 day would require about 9 months. Meshes from synaptic reconstructions can easily contain 10^5–10^6 polygons rather than several thousand, so even single simulations are not feasible in the absence of partitions. With partitions, however, such large-scale simulations are now routine.

Sources of Miniature Endplate Current Variability: Reconstruction and Simulation of Realistic Endplate Ultrastructure

Planar Junctional Fold Model

As outlined previously, MC simulations based on a simplified (planar) model of JFs at the NMJ (Fig. 15.13) are sufficient when comparing predictions to average values of experimental measurements, such as MEPC amplitude, rise time, and fall time. To address factors that underlie MEPC variability, the model must be more realistic, and in this section we introduce high-resolution reconstructions and simulations of the synaptic ultrastructure. To begin, we first establish a baseline for comparison by examining the variability predicted by the planar JF model itself.

The planar JF model (Fig. 15.13) represents a "thick section" through one nerve terminal and underlying muscle from a vertebrate NMJ (see Fig. 15.2). The real membrane topology is simplified to regular and constant dimensions, so the structure is characterized by the following parameters (typical values used for reptile or mammalian endplates are shown in parentheses, e.g., Matthews-Bellinger and Salpeter, 1978; Salpeter et al., 1984):

1. Primary cleft length and width (2–4 μm).
2. Primary cleft height and secondary cleft width (50 nm).
3. Distance between JFs (0.2–0.4 μm).
4. Depth of the JFs (0.5–1.0 μm).
5. AChR site density on the crests of the JFs (7000–10,000/μm^2).
6. Depth to which crest AChRs extend within JFs (0.2–0.3 μm).
7. Additional depth to which AChRs extend at reduced density (0.2–0.3 μm at circa 30% of crest density).

8. Uniform AChE site density throughout basal lamina planes centered within the primary (1500–2500/μm^2) and secondary (effectively double the primary cleft value; see Fig. 15.13) clefts.
9. Position of ACh release site.

Based on the size of a single AChR (circa 8.5 nm diameter; Unwin, 1998), the maximum packing density in postsynaptic membrane would be some 15,000/μm^2. This is considerably larger than quantitative values obtained with EM autoradiography, so even crest AChRs are unlikely to cover the entire membrane area. The actual microscopic distribution within a given area remains unknown owing to the limited resolution of experimental measurements. As a first approximation, in MCell simulations we set σ_{EG} (the global effector grid density) to a value near the maximum packing density, and then when AChR effector sites are

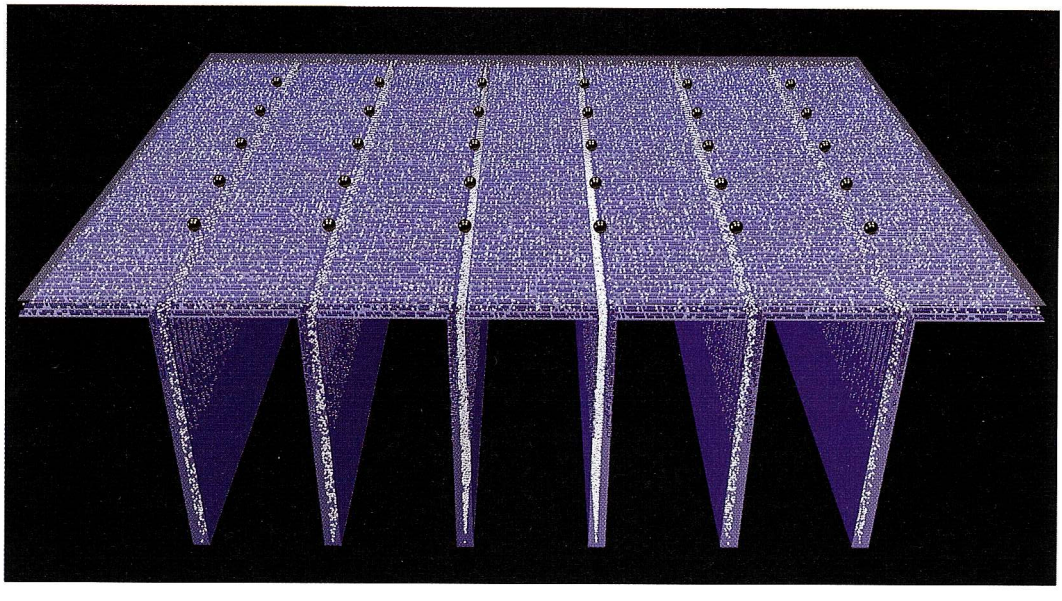

Figure 15.13. Simplified (planar) model of a vertebrate NMJ with JFs. Pre- and postsynaptic membranes (semitransparent and blue, respectively) are represented by rectangular planes (each rectangle is actually bisected into two triangles). The primary cleft is 2.0 × 2.7 μm in length and width and is 50 nm in height. The secondary cleft width is 50 nm; the JFs are 0.8 μm deep and are separated by 0.4 μm. AChRs (blue glyphs) are present at high density (7250/μm^2) on the crests of the JFs (i.e., to a depth of 0.22 μm) and at reduced density (70% less) for an additional 0.2 μm. Below that AChRs are absent. AChE active sites (white glyphs) are located in transparent planes that represent anchoring points in the basal lamina (1800/μm^2 in the primary cleft, and effectively 3600/μm^2 in the secondary clefts where the basal lamina doubles back as it follows the folded postsynaptic membrane). Black vesicles overlying the JFs represent 30 ACh release sites. The apparent linear "stripes" of AChR glyphs result from barycentric tiling of long, thin triangles (the bisected rectangles), as illustrated schematically in Fig. 15.4, and as seen in closer view in Fig. 15.15.

added at a density less than σ_{EG} their actual placement in different membrane regions reflects random choices between different available effector tiles (Fig. 15.4). The same is true for AChE sites in the basal lamina. If a constant amount of ACh (vesicle content, N_{ACh}) is released during each simulation, and fixed values are chosen for all of the parameters listed previously, then the only remaining sources of stochastic variability are ACh random walk movements and individual AChR and AChE reaction transitions. If the ACh release site is moved to different locations, then the regional differences in AChR and AChE positions become an added component of variability.

Figure 15.13 shows a planar JF model with 30 different ACh release sites located in active zones that are centered above 6 JFs (active zones generally are observed above the opening of a secondary cleft; see Fig. 15.2). Ten different simulations were run at each release site, using the AChR and AChE reaction mechanisms and rate constants shown in Fig. 6C,D. Exocytosis of ACh (i.e., diffusion through an expanding fusion pore) was simulated using a timesaving method that omits the vesicle and pore but reproduces the time course of release shown in Fig. 15.12. This method allows the use of a constant time step on the microsecond scale rather than an adaptive time step on the picosecond-to-nanosecond scale and hence reduces the required computer time by several orders of magnitude (Stiles et al., 1998).

To summarize the MEPC variability predicted by the planar JF model, the 10 individual MEPCs simulated for each release site were averaged together, and the resulting 30 traces are superimposed in Fig. 15.14A. The traces are very nearly identical (e.g., the coefficient of variation [CV] for peak amplitude is less than 1%). The mean amplitude is circa 1000 open AChR channels, and the difference between the minimum and maximum amplitudes is less than 40 channels (essentially the same result is obtained for each set of 10 MEPCs per release site; not shown).

For each of the 300 simulated MEPCs, ACh diffuses away from the release site and becomes diluted as it binds to AChRs and AChEs. The efficiency of binding therefore decreases over time and radial distance. A snapshot at the time of peak amplitude (Fig. 15.15A) shows a central area of double-bound open AChRs (yellow) surrounded by a sparse fringe of single-bound states (red), that is, the saturated disc of postsynaptic activation. The size of the saturated disc is not large enough to reach the edge of the primary cleft, but it is large enough to sample many AChRs over a radial distance of circa 0.2 μm in the primary and secondary cleft. The size of the saturated disc and postsynaptic response overwhelms noise that arises from stochastic single-channel behavior and regional membrane differences in AChR and AChE placement. Thus, on the scale of the saturated disc, the structure of the planar JF model is essentially constant and MEPCs show little variability.

When analogous simulations are run with AChE completely inhibited, the mean amplitude is 35% larger and the falling phase is prolonged (Fig. 15.14B). However, the CV remains very small (2.6%), and the 30

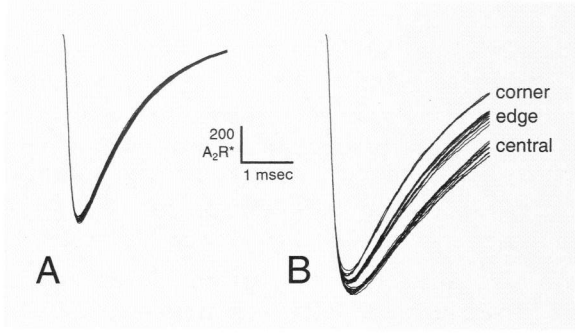

Figure 15.14. MEPC variability is minimal for the planar JF model and 30 ACh release sites shown in Fig. 15.13. In both *A* and *B,* 30 MEPCs are superimposed (one per release site, each an average of 10 individual simulations in which 6200 ACh molecules were released, Δt = 1.0 μsec). In *A,* AChE was normally active (reaction mechanism shown in Fig. 15.6D), and in *B,* AChE activity was completely inhibited (k_{+1} in Fig. 15.6D was set to zero, so ACh could never bind). The reaction mechanism for AChR activation was as shown in Fig. 15.6C, and MEPC amplitude is expressed as the number of receptors in the double-bound, open conformation (A_2R^*). In *B,* the mean amplitude is circa 35% larger than in *A,* and the 30 MEPCs fall into three groups according to the position of the ACh release site (corner, edge, or central; see text and Fig. 15.15).

traces fall into three easily discernible categories based on their amplitudes and fall times. The smallest traces are also those with the shortest duration, and they correspond to the four corner release sites. The traces that are intermediate in size and decay time correspond to the 14 edge (noncorner) positions, and the largest, slowest-decaying traces correspond to the 12 central release sites.

With AChE inhibited, the full amount of released ACh (N_{ACh}) spreads radially and binds to additional AChRs during formation of the saturated disc. For release from a central location, the additional AChRs are readily available in all directions, so the radius of the disc is somewhat larger (Fig. 15.15B) and the increased peak amplitude is reached somewhat later. During the falling phase, ACh binds repeatedly and hence diffuses and dilutes slowly (buffered diffusion; Katz and Miledi, 1973). Although the efficiency of channel opening is low, additional openings are frequent enough to prolong the fall time circa threefold. With release from a corner or edge site, peak amplitude increases less because a significant fraction of spreading ACh escapes from the primary cleft even during the rising phase. More escapes during the falling phase, which reduces buffered diffusion and attenuates the prolongation of fall time.

The variability of quantal endplate signals has been an integral factor in classical quantal analysis for many years (del Castillo and Katz, 1954; Redman, 1990; Edwards, 1995a,b) and is markedly larger than the variability predicted by the planar JF model. Experimental MEPC amplitudes vary by a factor of two to three, and the distribution is approximately

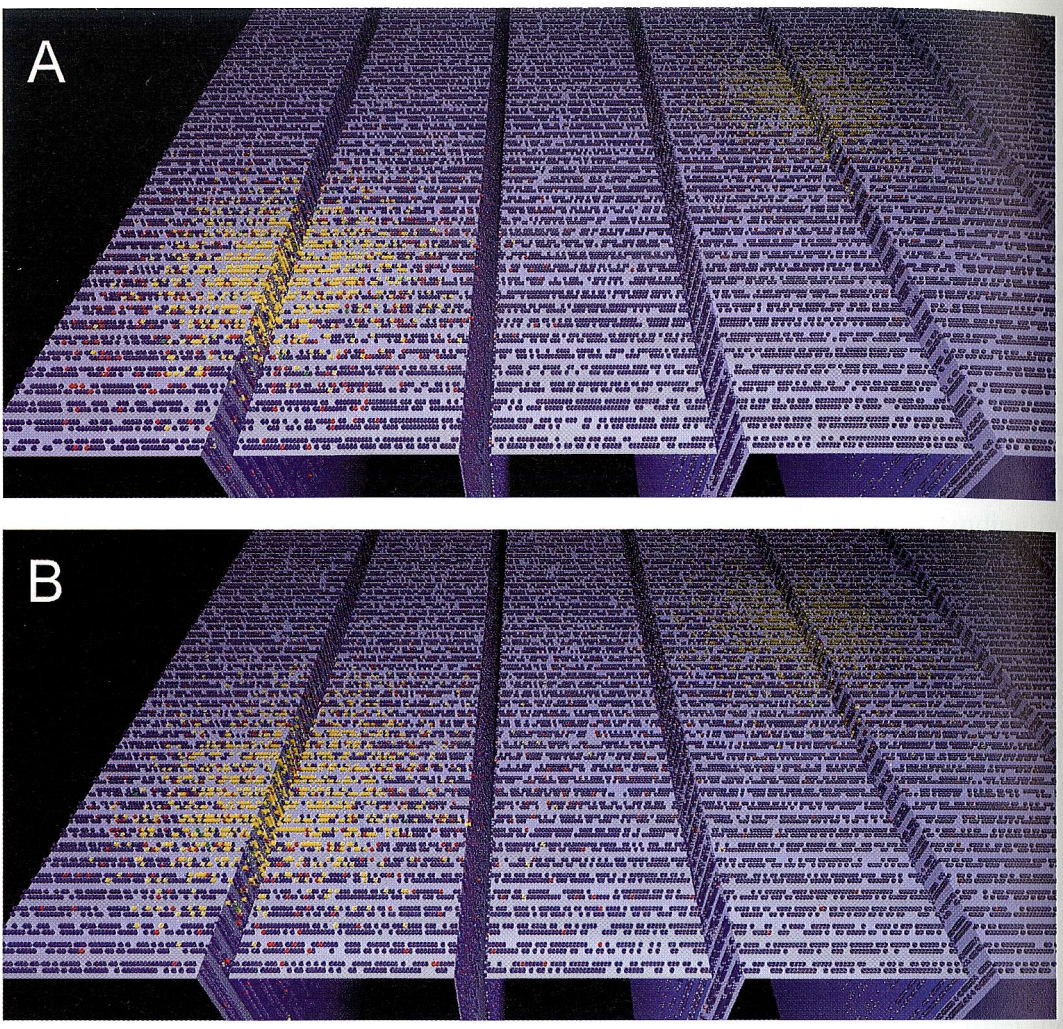

Figure 15.15. Appearance of the saturated disc in the planar JF model. For this illustration, ACh was released from two sites simultaneously (central and corner), and the presynaptic membrane and AChE sites are omitted for clarity.

(A) Snapshot at peak amplitude with AChE active (circa 300 μsec after onset of ACh release). AChR glyphs are color-coded according to their reaction state (AR^1 and AR^2, red; A_2R, green; A_2R^*, yellow; see Fig. 15.6C). ACh molecules are tiny dots. If bound, they have the same color as the corresponding AChR glyphs. If unbound, they are cyan. The radial extent of saturated disc formation is small enough that the edge of the primary cleft space has no effect on MEPC variability (see text and Fig. 15.14A).

(B) Snapshot at peak amplitude with AChE inhibited (circa 490 μsec). The saturated disc has spread farther than it does with active AChE, so edge effects are apparent for peak amplitude and fall time (see text and Fig. 15.14B). Single-bound AChRs arising from the two release sites show clear overlap.

Gaussian (broader and shifted slightly to larger values after AChE inhibition). It has mostly been assumed that this variability arises from differences in N_{ACh} from one vesicle to another (Edwards, 1995a), but the planar JF model can be used to suggest other alternatives. For example, small changes (much less than twofold) in primary cleft height, JF width, or global AChR density can all affect MEPC amplitude to an extent that greatly outweighs the stochastic variability illustrated previously. In addition, all of these factors introduce opposing changes in amplitude and rise time (e.g., an increase in primary cleft height would decrease amplitude but increase rise time). Changes in N_{ACh} or the distance between JFs, on the other hand, cause amplitude and rise time to change in the same direction. Experimental MEPCs show little or no correlation between amplitude and rise time (Land et al., 1980; Bartol, 1992; J. Stiles, unpublished data), so presynaptic factors (i.e., N_{ACh}, ACh exocytosis) and postsynaptic architecture must both contribute significantly to MEPC variability, with offsetting influences on amplitude and the time course of the rising phase. With AChE active, MEPC fall time is almost exclusively determined by the apparent open time of the AChR channel (Anderson and Stevens, 1973; Anglister et al., 1994; Stiles et al., 1999), so variability in single-channel kinetics from one AChR to another will also be required for a complete model of MEPC variability.

Curved and Branched Junctional Fold Model

As a first step toward modeling these complexities, we designed a more realistic "thick section" of NMJ that has curved and branched JFs, but that otherwise can easily be compared to the planar JF model. A portion of pre- and postsynaptic membrane contours was traced from a TEM image of rat diaphragm NMJ (Fig. 15.16A), and the length of primary cleft, number of JFs, and spacing between JFs were similar to the corresponding parameters in the planar model. The fold structure was morphed smoothly to obtain additional successive "sections," which then were reconstructed into optimized pre- and postsynaptic meshes for MCell simulations (circa 3400 and 25,000 triangles in the nerve and muscle membrane meshes, respectively; Fig. 15.16B). As shown in Fig. 15.16D, the muscle membrane was clipped into pieces representing crest, intermediate, and deep JF regions, and AChR effector sites were added to the top two regions (circa 91,000 total), as had been done for the planar JF model. A third polygon mesh containing AChE sites (circa 59,000) was created to model the basal lamina and followed the contour of the postsynaptic membrane (Fig. 15.16C). Thirty ACh release sites were placed in active zones above the folds (Fig. 15.16C,D), and ACh exocytosis was simulated using the timesaving method described previously.

Ten MEPCs were simulated and averaged for each release site of the branched JF model, and the resulting 30 traces are shown superimposed in Fig. 15.17A. Comparison of these results to those for the planar JF model (Fig. 15.14A) shows that the MEPC variability is markedly

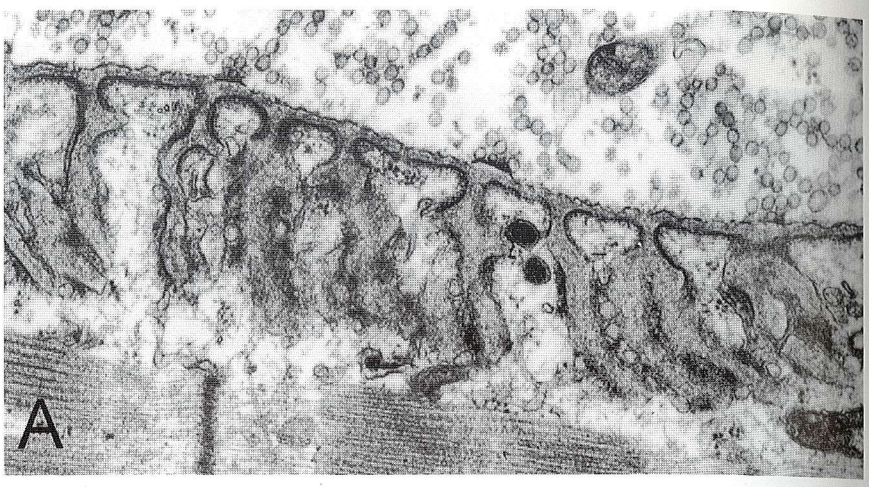
A

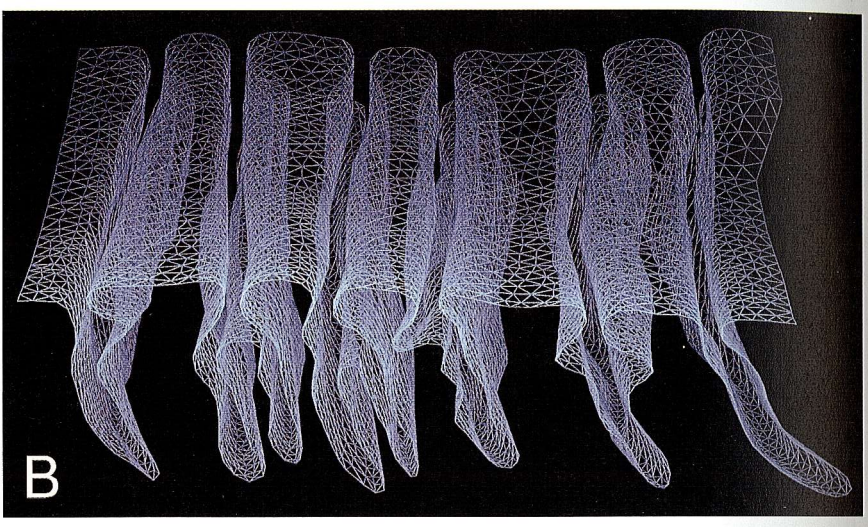
B

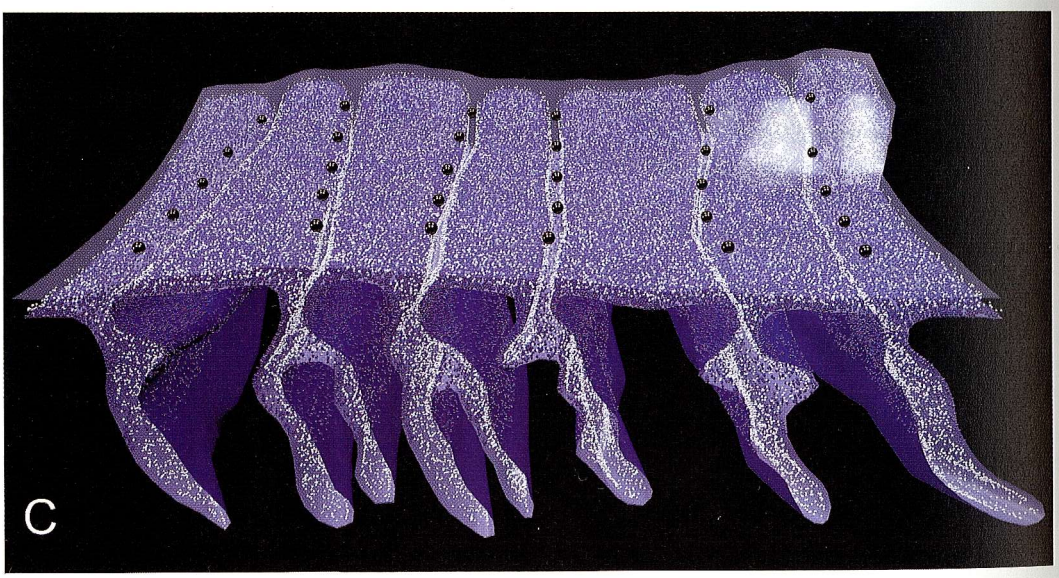
C

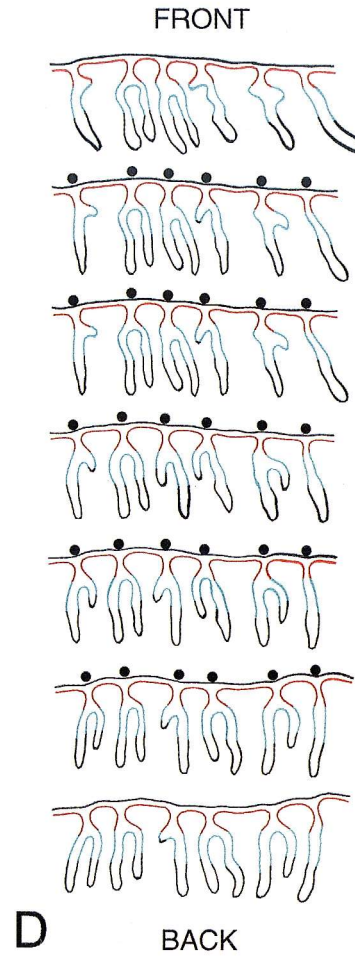

Figure 15.16. Model of a vertebrate NMJ with curved and branched JFs.

(A) Typical TEM of rat diaphragm NMJ. Three active zones are clearly seen above the openings of JFs. From Peters et al. (1991), used by permission of Oxford University Press, Inc.

(B) Wireframe image of the optimized mesh created after tracing and morphing a portion of the postsynaptic membrane shown in *A*.

(C) Pre- and postsynaptic membranes, AChR and AChE glyphs, and 30 ACh release sites visualized as described previously for the planar JF model (Fig. 15.13). The contour of the basal lamina (1800 AChE sites/μm^2) follows that of the postsynaptic membrane throughout the branched and variable JFs. The postsynaptic membrane was subdivided into crest, intermediate, and deep JF regions, as shown in *D,* and the density of AChRs in each region was the same as for the planar JF model. The apparently random positions of AChR glyphs reflect barycentric tiling of the optimized mesh, which contains nearly equilateral triangles (*B;* and see Fig. 15.4A).

(D) JF structure and ACh release sites. The pre- and postsynaptic membranes shown in *C* were cut in a manner analogous to TEM thin sections (40 nm). At the top is the leading edge (front) section, followed by those sections that included a row of ACh release sites, and the final (back) section. The postsynaptic membrane is color-coded according to JF region (and therefore AChR density): crest, red; intermediate, cyan; deep, black. The line thickness along each contour is determined by the orientation of the membrane relative to the plane of section.

increased. The CV is 6%, that is, more than sevenfold larger than the previous result, the range of amplitudes is larger by more than fivefold, and a relative independence of amplitude and rise time is qualitatively evident. The mean amplitude is reduced by some 25% and reflects increased diffusion and dilution space within the curved and branched secondary cleft contours. The variability for each set of 10 MEPCs per release site was no different than that for the planar JF model (not shown), so the results shown here originate entirely from geometric differences between release sites. The relationship between MEPC amplitude and the detailed structure underlying each release site (see contours of Fig. 15.16D) is not easy to predict, as some of the largest and smallest MEPCs occurred at corner and edge positions, over single and branched JFs. In essence the MEPC amplitude is very sensitive to the cleft volume within and around the region of saturated disc formation, and this 3-D parameter is very difficult to estimate by eye from membrane contours.

When AChE inhibition is simulated (Fig. 15.17B), the mean amplitude is 38% larger than with AChE active (Fig. 15.17A). This relative change is almost exactly the same as that described previously for the planar NMJ model (35%), but the range and variability of amplitudes are markedly increased (CV of 7.6%, about threefold larger; compare Fig. 15.17B to Fig. 15.14B). Neither the amplitudes nor the falling phases shown in Fig. 15.17B can be separated into nonoverlapping groups on the basis of corner, edge, or central ACh release position. In addition, the amplitude range nearly overlaps the range obtained with normal AChE activity (Fig. 15.17A). When AChE inhibition is simulated using the branched rather than planar JF model, diffusing ACh travels farther into the larger available cleft volume and therefore "samples" more geometric variability. This diminishes the influence of the primary cleft boundary and broadens and smoothes the distributions of MEPC size and time course to resemble experimental distributions more closely.

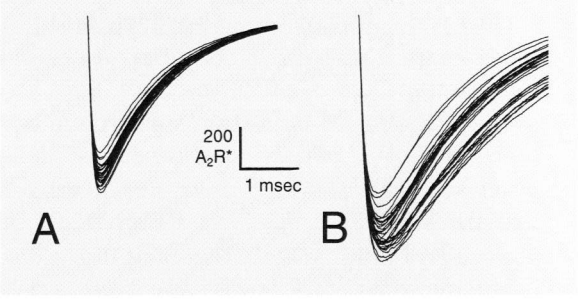

Figure 15.17. MEPC variability for the NMJ model with curved and branched JFs. As in Fig. 15.14, 30 MEPCs (one averaged trace per ACh release site) are superimposed in *A* (AChE active) and *B* (AChE inhibited). The mean amplitude is circa 38% larger in *B* than in *A*, that is, about the same relative increase as obtained with the planar JF model and AChE inhibition. However, the MEPC variability is many times larger than that obtained with the planar JF model (see text). Δt = 1.0 μsec.

Neuromuscular Junction Reconstruction and Simulation

Even with N_{ACh} held constant (i.e., assuming no variation in the amount of ACh released per quantal event), the variability introduced by the branched JF model represents an appreciable fraction of experimental MEPC variability (e.g., 30–50% based on range of amplitudes). Hence this model illustrates very well the importance of architectural realism in synaptic simulations. However, the branched JF model itself remains a simplification (surprisingly so), and therefore it also illustrates very well the need for high-resolution, quantitative reconstructions of synaptic architecture. It is considerably more difficult to create such reconstructions for use with simulations than it is to create them for imaging and morphometrics, and we will detail our methods and large-scale efforts elsewhere. We conclude here with an illustrative example and briefly compare preliminary results from MCell simulations to those obtained with the branched JF model.

Since the distance across primary and secondary cleft spaces is about 50 nm, the resolution for reconstructions must be about 10 nm or better in all three dimensions for use with simulations. On the other hand, the overall size of the reconstruction is on the order of microns in each dimension, so the scale of the problem is quite large and presents many technical challenges. In essence, creation of a reconstruction for use with MCell simulations entails three steps: (1) generation of a high-resolution EM data set for a volume of tissue, (2) extraction of membrane or other surfaces of interest from the volumetric data set, and (3) subdivision of the surfaces as needed, to add simulation objects such as ligand release sites and different populations of effector sites (e.g., subdivision of JFs according to AChR density).

The conventional approach to step 1 is serial TEM sections, but typically even the thinnest sections (say, 40 nm) are thicker than the desired resolution, and as section thickness decreases the section uniformity and number of serial sections can become problematic. EM tomography ultimately may be a better approach and is becoming more accessible, and the specific application of such methods to MC simulations is an important area for future research. Step 2 requires both the identification of the surfaces and their subsequent transformation into optimized polygon meshes, and such problems are presently the focus of much computer science and graphics research, particularly for highly convoluted structures like cell membranes. Step 3 is likewise a present-day computer science and graphics problem, and it poses particular difficulties because of the need for interactive control over very large-scale structures.

For the example illustrated here, we reconstructed a length of nerve terminal and postsynaptic membrane from a mouse sternomastoid NMJ. Approximately 20 sequential TEM sections were cut to a thickness of 100 nm to ensure high uniformity, and 7 were chosen for the reconstruction. The resulting mesh thus had an aggregate thickness of 0.6 μm, that is, several times the diameter of a saturated disc. Figure 15.18A (inset)

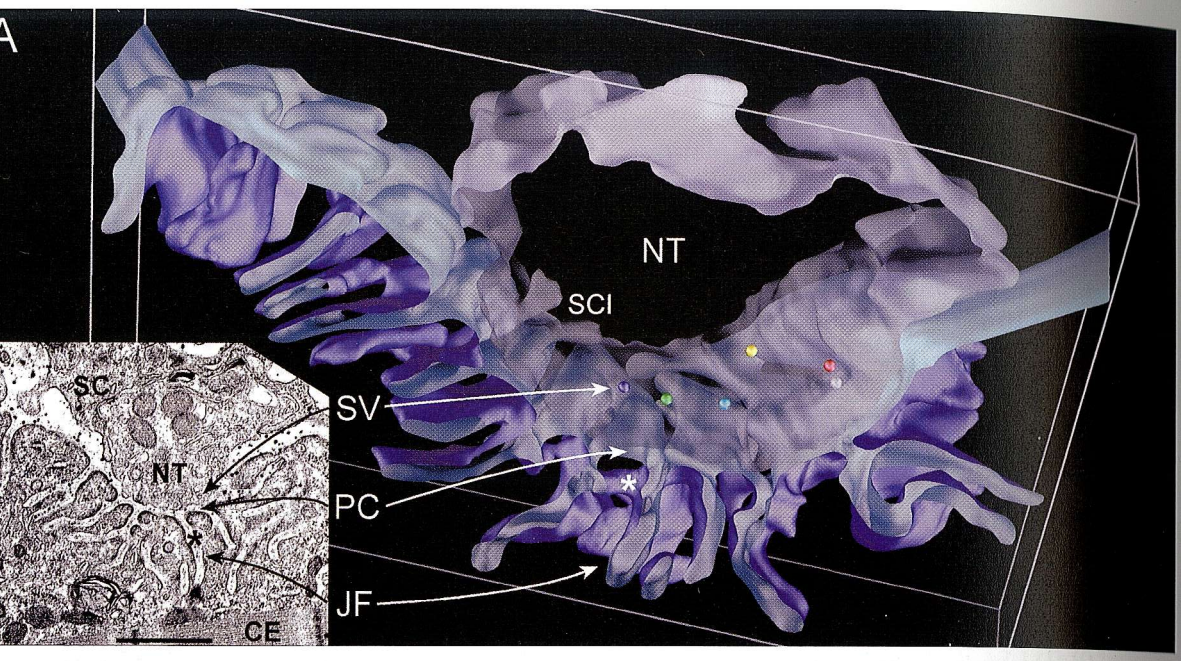
A
NT
SCI
SC
NT
SV
PC
JF
CE

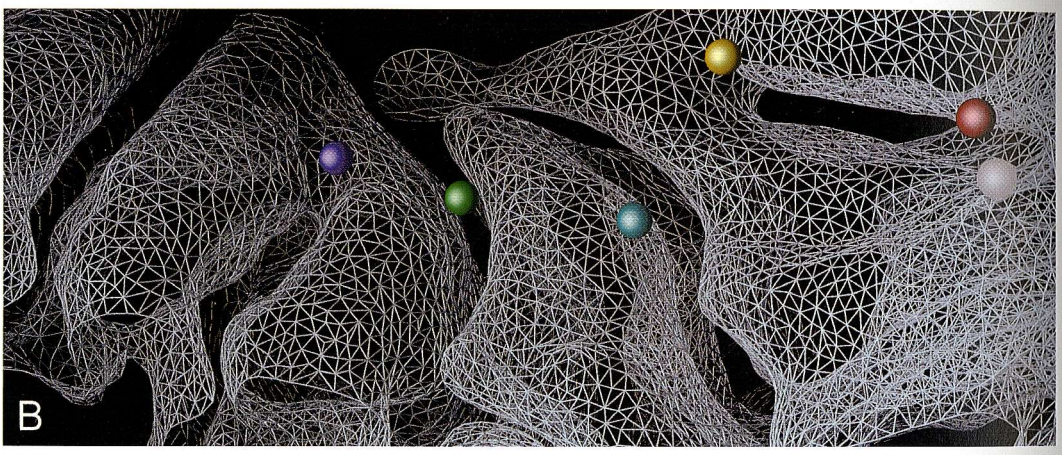
B

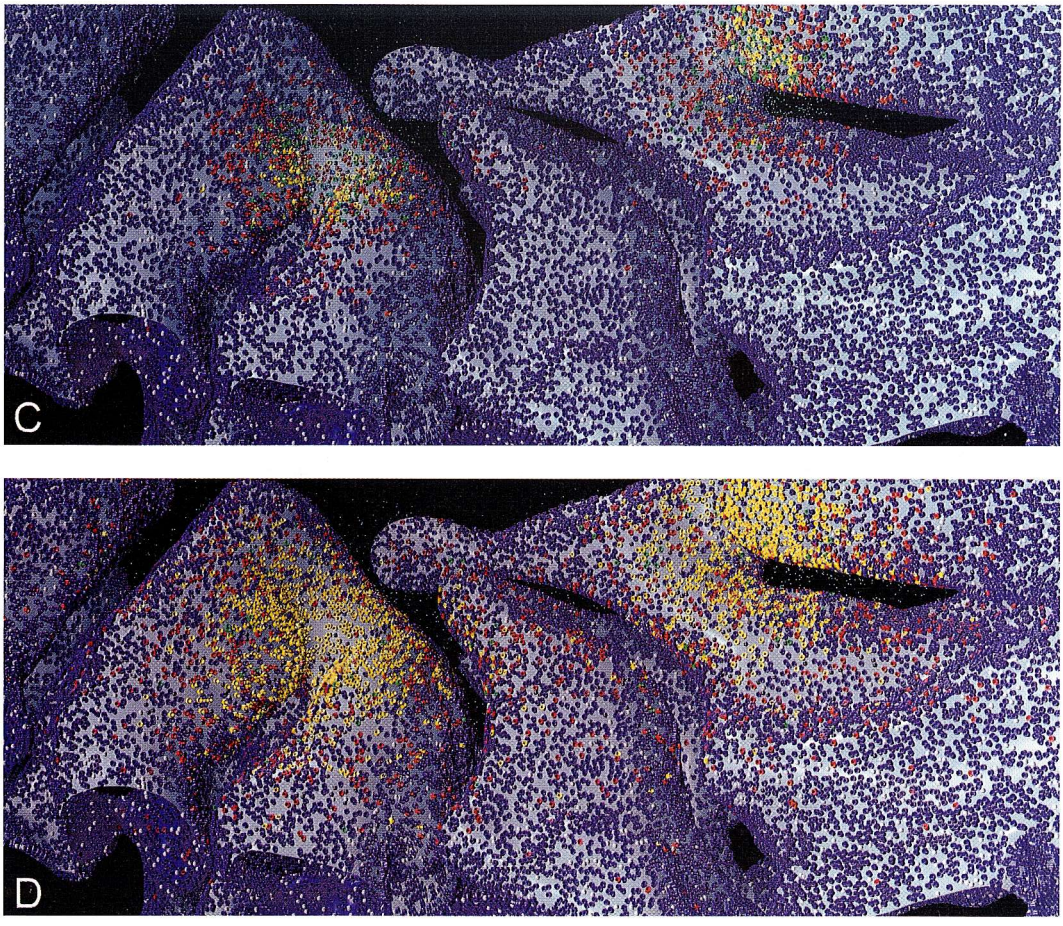

Figure 15.18. Simulation of MEPCs in a high-resolution, partial reconstruction of mouse sternomastoid NMJ.

(A) The inset shows a TEM image from one section used for the reconstruction. CE, contractile elements; JF, junctional fold; NT, nerve terminal; PC, primary cleft; SC, Schwann cell; SV, synaptic vesicle. Scale bar = 1 μm. The segment of reconstructed nerve terminal is shown in translucent gray, and six ACh release sites are indicated by color-coded synaptic vesicles that correspond to the six color-coded MEPCs shown in Fig. 15.19. Extra- and intracellular faces of the postsynaptic muscle membrane are light and dark blue, respectively, and the bounding box is $4.2 \times 0.6 \times 2.5$ μm. SCI, Schwann cell process invaginations. Asterisks mark the position of a tunnel between JFs.

(B) Close-up image of the ACh release sites above the postsynaptic membrane, shown as a wireframe view of the optimized mesh.

(C–D) Illustrative snapshots of MEPC generation for the yellow and blue ACh release sites, 100 μsec (*C*) and 400 μsec (*D*) after onset of release. AChRs and AChE active sites were distributed uniformly over the postsynaptic membrane at 7250 and 1800/μm^2, respectively. The colors for AChR and ACh glyphs are the same as in Fig. 15.15. Unbound AChE sites are shown as white spherical glyphs, and bound AChE states (Fig. 15.6D) are black.

shows a micrograph from one of the sections, and Fig. 15.2B shows another representative TEM view of a mouse sternomastoid NMJ. In contrast to textbook depictions, the JF structure and disposition of thickened postsynaptic membrane are extremely complicated, and tunnels can even cross from one secondary cleft to another (asterisk in Fig. 15.18A).

The seven sections chosen for the reconstruction were digitized, and the pre- and postsynaptic membrane contours were traced as smooth curves in each. The positions of synaptic structures can change a great deal from one TEM section to the next, and such changes can markedly degrade the output of surface reconstruction algorithms. To overcome this problem, a method was devised to interpolate between the contours of adjacent sections and thus in effect create additional "sections" at finely spaced intervals between the originals.[11] After interpolation, a total of 121 "sections" were obtained at 5-nm intervals, containing smoothly curved pre- and postsynaptic membrane contours that changed very little from one section to the next. The sections were then used to create corresponding images of the contours with a pixel scale of 5 nm, and the resulting "stack" of images at $5 \times 5 \times 5$-nm final resolution was passed through a "marching cubes" surface reconstruction algorithm (Schroeder et al., 1998) that in our experience is the most reliable for highly convoluted structures. The initial meshes obtained for the pre- and postsynaptic membranes each contained several million triangles, and they were subsequently decimated (reduced to fewer triangles) and optimized for MCell simulations without appreciable degradation of topology. The final meshes for the nerve and muscle surfaces contained 20,000 and 80,000 triangles, respectively.

Figure 15.18A shows the reconstructed nerve and muscle membranes and their overall dimensions. To those preconditioned by typical cartoons of vertebrate NMJs, the structure is exceedingly complex. Because of numerous twists, pockets, and interconnections at various depths, the structure of the JFs is closer to that of a sponge than a pleated sheet. A close-up view of the optimized mesh for the muscle membrane is shown in Fig. 15.18B, together with six synaptic vesicles positioned at different possible ACh release sites above secondary cleft openings.

The next level of detail for this reconstruction would be realistic distributions and densities of AChR and AChE sites. However, to illustrate the isolated effect of synaptic topology on MEPC variability, we added AChR effector sites at uniform crest density over the entire muscle surface and then intermixed AChE sites onto the muscle surface as well. Exocytosis of ACh was simulated as described previously for the planar and branched JF models, and Fig. 15.18C,D shows different stages of saturated disc formation during release from two of the six vesicles indicated in Fig. 15.18A,B. Individual color-coded MEPCs that correspond to the six different release sites are illustrated in Fig. 15.19, and the range of amplitudes is almost as large as the range obtained with 30 different release sites and the branched JF model (Fig. 15.17A). Although

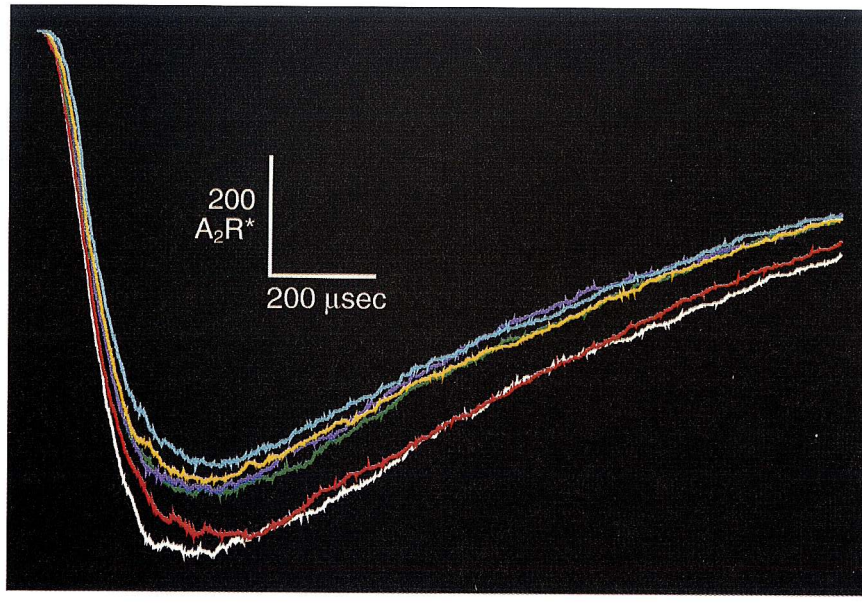

Figure 15.19. Preliminary examples of MEPC variability arising from highly realistic postsynaptic topology at the mouse sternomastoid NMJ. Individual color-coded MEPCs are shown, corresponding to the ACh release positions indicated in Fig. 15.18A,B (Δt = 0.5 μsec). Whereas classical assumptions have mostly attributed MEPC variability to differences in the amount of ACh released from each synaptic vesicle, these examples, based only on a thin strip of reconstructed tissue, show that significant differences in amplitude and rise time can arise just from local differences in cleft architecture.

the yellow release site is positioned near the edge of the primary cleft space, the corresponding MEPC is not the smallest of the group. The remaining release sites are positioned about midway across the thickness of the structure, and there is no easily discernible relationship between their positions, the surrounding JF structure, and the relative sizes of the MEPCs. In addition, there is no apparent correlation between MEPC amplitude and the time-to-peak. Therefore, preliminary results obtained with this high-resolution reconstruction substantiate the results described previously for the branched JF model.

Close examination of TEM sections for mouse sternomastoid NMJs (e.g., Figs. 15.18A [inset] and 15.2) shows that the depth and disposition of thick, ostensibly AChR-rich, postjunctional membrane is highly variable, and that vesicles and active zones can be positioned at the "edge" of the nerve terminal where the height of the primary cleft can increase markedly. The addition of these factors to reconstructions of extended thickness (at least 4–5 μm) will allow a quantitative description of MEPC variability (with and without AChE inhibition) arising from postsynaptic structural variations. Thereafter distributions for additional pre- and postsynaptic factors (e.g., N_{ACh}, vesicle volume [which would affect the

rate of ACh release], and single channel rate constants) can be added to the model in order to deconvolve their contribution to the total observed variability of amplitude, rise time, and fall time, and explain correlations or the absence of correlations between the quantal size and time course.

A Brief Look to the Future

In this chapter we have reviewed and illustrated MC methods for simulation of molecular diffusion and chemical reaction in 3-D subcellular environments. Our focus was synaptic physiology and detailed structural realism. Large-scale reconstructions of complex endplate morphology presently underlie ongoing simulations of normal and pathological neuromuscular function.

Although 3-D reconstructions are becoming increasingly common in biological research, the combination of reconstruction and simulation is in its infancy. Quantitative simulations require reconstructions with very high resolution and accuracy, and thus the reconstruction and model design become significant computational challenges in and of themselves. The design and use of such detailed quantitative models drives the acquisition of more accurate experimental data and (particularly with highly realistic MC models) often changes the way one thinks about the structure and function of the modeled system. This in turn leads to different avenues of experimental investigation, the results of which then can be used to test or extend the model. An excellent case in point is detailed relationships between synaptic current size and time course, which can be used to identify and constrain pre- and postsynaptic parameters that contribute to synaptic variability and plasticity. Once this approach has been worked out in a relatively simple system (e.g., the NMJ), it may be applied in more complex settings (e.g., a reconstructed volume of neuropil).

Computational power continues to grow exponentially and is expected to do so throughout the foreseeable future. New algorithms will take advantage of such increased power and will continue to add new levels of realism to MC simulations. For example:

1. Bimolecular associations, as described here for diffusing ligand molecules and fixed effector sites, will be extended to include interactions between multiple diffusing species (e.g., Ca^{2+}, Ca^{2+}-sensitive dyes, and mobile Ca^{2+}-binding proteins).
2. Surface properties such as membrane potential will be added and combined with electric field and pressure gradient modifications to diffusion algorithms, so that classical transport physiology and cellular excitation can be simulated at the level of stochastic 3-D interactions.
3. Biomechanical properties will be added to components of models, to simulate cellular motility and the active intracellular trafficking of molecules and organelles.

Such new and existing modeling capabilities, together with a rapidly expanding experimental data base of 3-D structure, molecular constituents, biochemical pathways, and physiological measurements, will help provide quantitative answers to many existing questions centered on synaptic plasticity, crosstalk, modulation, and functional relationships between neurons and glia. Increasingly realistic models may also help to identify previously unforeseen principles of peripheral and central synaptic function. Perhaps in time functional analogies will be drawn between JFs at the NMJ, perforated spine synapses in the brain, and intersynaptic regions between dendritic spines—all structures that provide interspersed receptive and nonreceptive postsynaptic area and cleft space. At present it seems that all may somehow reflect or influence neurotransmitter receptor localization and metabolism (e.g., endplate AChR turnover; Akaaboune et al., 1999; Salpeter, 1999) or glutamate receptor mobilization and recruitment during long-term potentiation of excitatory hippocampal synapses (Shi et al., 1999). Another outcome of interleaved experimental and realistic modeling studies could be guided development of new clinical interventions for peripheral and central nervous system diseases.

Appendix: Symbols

A_{ET}	Area of effector tile
A_{ME}	Area of mesh element
C_L	Ligand concentration
D_L	Ligand diffusion constant
Δt	Monte Carlo time step
E	Effector site
h	Exocytotic pore height
κ	Random number
k	Rate constant for unimolecular transition
k_+	Rate constant for bimolecular association
L	Ligand
l_r	Random walk radial step length
$\bar{l}_r$	Random walk average radial step length
$\bar{l}_\perp$	Random walk average step length along direction perpendicular to a mesh element
N_{ACh}	Number of acetylcholine molecules in a synaptic vesicle
N_B	Average number of ligand molecules that bind to an effector site during Δt
N_{ET}	Number of effector tiles on a mesh element
N_H	Average number of ligand molecules that hit an effector tile during Δt
p	Probability
p_b	Monte Carlo binding probability, obtained conceptually from N_B/N_H
p_k	Monte Carlo probability of a unimolecular transition
r	Radial distance, or exocytotic pore radius
V_{ET}	Volume "above" and "below" effector tile, product of area A_{ET} and height $2(\bar{l}_\perp)$

Acknowledgments

We thank the following for excellent technical assistance: Maria Szabo for electron microscopy, Philip Davidson for 3-D reconstructions, and Krishna Juluri for MCell simulations. J.R.S. and T.M.B. also personally acknowledge the invaluable assistance of Mark Stiles and Bruce Land in the early years of Monte Carlo code development on VAX and IBM computer systems, respectively. This work is supported by NIH grants K08 NS01776 and RR-06009 (J.R.S.), NSF grant IBN-9603611 (T.M.B. and T.J.S.), and NIH grants NS09315 and GM10422 (M.M.S.).

Notes

1. Based on observed distances between synaptic densities in 3-D reconstructions (e.g., Ventura and Harris, 1999).

2. <http://www.mcell.cnl.salk.edu> and <www.mcell.psc.edu>.

3. MCell's MDL allows simulation models to be archived and exchanged in readable text. An MDL Reference Guide and tutorial examples are available at the MCell Web sites given in note 2.

4. Random numbers are used to choose step lengths and directions, and to make other choices, and the computer time required to calculate random numbers is a significant fraction of the time required to run a simulation. MCell includes a self-contained cryptographic-quality random number generator that ensures identical results across different computer platforms and is optimized for speed in various ways (e.g., the bits obtained from calculation of a single random number are subdivided so that two or more decisions can be made for the price of one).

5. In computer graphics, ray tracing entails following a light ray through successive surface intersections and reflections, and ray marching is a special case in which some property of the ray (e.g., intensity) is decremented after each intersection. By analogy, MCell employs highly optimized ray tracing and ray marching algorithms for ligand movements.

6. Software packages for surface reconstruction and mesh optimization (including adaptation to nearly equilateral triangles) are freely available in many forms, but their design, reliability, and usefulness are highly variable. Additional details can be found at the Web sites given in note 2.

7. If a reaction that consumes ligand is used, such as that shown for AChE hydrolysis of ACh in Fig. 15.6D, then the ligand consumption can be balanced by introducing additional effector sites that produce ligand at the necessary rate. The simulation thus is run under steady-state rather than equilibrium conditions.

8. Each simulation was begun with all rate constants in the reaction mechanism set to zero, so no transitions would occur and the initial state of the effector sites would be preserved. The ligand molecules were introduced at a point in the center of the sphere, and the first checkpoint was reached when the ligands had diffused to uniform average concentration. The run was then continued from this checkpoint with all rate constants changed from zero to their desired values, so that the reaction could either proceed to equilibrium or remain at equilibrium, depending on the initial state of the effector sites. To simulate a relaxation, a second checkpoint was used to stop the run, set all rate constants back to zero, and introduce additional free ligand molecules, which then diffused to uniform concentration together with the pre-existing ligand. A final checkpoint reset the rate constants so that the relaxation would proceed.

9. But not, for example, an order of magnitude smaller than r, which would likely be the case with a simpler random walk algorithm based on a fixed step

length and movements on a lattice. Equivalent accuracy with the simpler method (which would not execute any faster) thus would probably require a step length about 4-fold smaller than $\bar{l}_r$. Because step length scales with $\sqrt{\Delta t}$, the simulation would require about 16-fold more time step iterations and a corresponding increase in computer time.

10. A reflective plane was added to cut across the pore where it joins the vesicle. The ACh molecules inside the vesicle thus could not escape and were allowed to diffuse until they became uniformly dispersed. The simulation then was halted and restarted from this checkpoint without the reflective plane, so that ACh molecules could diffuse through the pore and into the cleft space.

11. Automated interpolation of highly irregular, convoluted contours is not generally possible because there is no simple way to keep corresponding portions, or segments, of the contours in register. When registration errors occur, the interpolated surface is likely to twist and pass through itself, which will ruin a reconstruction that is to be used with simulations. In brief, our method for interpolation entails (1) animating the sequence of original TEM images, because the correspondence between structures in different sections is much easier to grasp when the structures are seen "in motion"; (2) hand-subdivision of the complex contours of each section into shorter segments with simple shapes (e.g., a portion of a single JF); and (3) automated linear interpolation between corresponding segments of adjacent contours, to create entire new contours between those of the original sections.

References

Akaaboune, M., Culican, S. M., Turney, S. G., Lichtman, J. W. (1999). Rapid and reversible effects of activity on acetylcholine receptor density at the neuromuscular junction *in vivo*. *Science* 286:503–507.

Albuquerque, E. X., Barnard, E. A., Porter, C. W., Warnick, J. E. (1974). The density of acetylcholine receptors and their sensitivity in the postsynaptic membrane of muscle endplates. *Proc. Natl. Acad. Sci. USA* 71:2818–2822.

Anderson, C. R., Stevens, C. F. (1973). Voltage clamp analysis of acetylcholine produced end-plate current fluctuations at frog neuromuscular junction. *J. Physiol.* 235:655–691.

Anglister, L., Stiles, J. R., Salpeter, M. M. (1994). Acetylcholinesterase density and turnover number at frog neuromuscular junctions, with modeling of their role in synaptic function. *Neuron* 12:783–794.

Apel, E. D., Merlie, J. P. (1995). Assembly of the postsynaptic apparatus. *Curr. Opin. Neurobiol.* 5:62–67.

Barbour, B., Hausser, M. (1997). Intersynaptic diffusion of neurotransmitter. *Trends Neurosci.* 20:377–384.

Barnard, R. J., Wieckowski, J., Chiu, T. H. (1971). Cholinergic receptor molecules and cholinesterase molecules at mouse skeletal muscle junctions. *Nature* 234:207–209.

Barrow, G. M. (1981). *Physical Chemistry for the Life Sciences.* New York: McGraw-Hill.

Bartol, T. M., Jr. (1992). A study of miniature endplate current generation at the vertebrate neuromuscular junction using electrophysiology and Monte Carlo simulation. Ph.D. thesis, Department of Neurobiology and Behavior, Cornell University.

Bartol, T. M., Jr., Land, B. R., Salpeter, E. E., Salpeter, M. M. (1991). Monte Carlo simulation of MEPC generation in the vertebrate neuromuscular junction. *Biophys. J.* 59:1290–1307.

Bennett, M. R., Farnell, L., Gibson, W. G. (1995). Quantal transmission at purinergic synapses: stochastic interaction between ATP and its receptors. *J. Theor. Biol.* 175:397–404.

Bennett, M. R., Farnell, L., Gibson, W. G. Lavidis, N. A. (1997). Synaptic transmission at visualized sympathetic boutons: stochastic interaction between acetylcholine and its receptors. *Biophys. J.* 72:1595–1606.

Bennett, M. R., Farnell, L., Gibson, W. G. (1998). On the origin of skewed distributions of spontaneous synaptic potentials in autonomic ganglia. *Proc. R. Soc. London Ser. B* 265:271–277.

Boudier, J. L., Le Treut, T., Jover, E. (1992). Autoradiographic localization of voltage-dependent sodium channels on the mouse neuromuscular junction using ^{125}I-alpha scorpion toxin. II. Sodium distribution on postsynaptic membranes. *J. Neurosci.* 12:454–466.

Bower, J. M., Beeman, D. (1995). *The Book of GENESIS: Exploring Realistic Neural Models with the GEneral NEural SImulation System.* Santa Clara, Calif.: TELOS.

Ceccarelli, B., Hurlburt, W. P., Mauro, A. (1973). Turnover of transmitter and synaptic vesicles at the frog neuromuscular junction. *J. Cell Biol.* 57:499–524.

Clements, J. D. (1996). Transmitter timecourse in the synaptic cleft: its role in central synaptic function. *Trends Neurosci.* 19:163–171.

Cornell, W. D., Cieplak, P., Bayly, C. I., Gould, I. R., Merz, K. M., Jr., Ferguson, D. M., Spellmeyer, D. C., Fox, T., Caldwell, J. W., Kollman, P. A. (1995). A second generation force field for the simulation of proteins and nucleic acids. *J. Am. Chem. Soc.* 117:5179–5197.

Couteaux, R. (1946). Sur les gouttières synaptiques du muscle strie. *C. R. Soc. Biol. (Paris)* 140:270–271.

Couteaux, R. (1955). Localization of cholinesterases at neuromuscular junctions. *Int. Rev. Cytol.* 5:335–375.

Couteaux, R. (1958). Morphological and cytochemical observations on the postsynaptic membrane at motor end-plates and ganglion synapses. *Exp. Cell Res.* 5(Suppl.):294–322.

Del Castillo, J., Katz, B. (1954). Quantal components of the endplate potential. *J. Physiol.* 124:560–573.

DeRobertis, E., Pellegrino DeIraldi, A., Rodriguez, G., Gomez, C. J. (1961). On the isolation of nerve endings and synaptic vesicles. *J. Biophys. Biochem. Cytol.* 9:229–235.

Doyere, L. (1840). Mémoire sur des tardigrades. *Ann. Sci. Nat. Zool.* 14:269–361.

Eccles, J. C., Jaeger, J. C. (1958). The relationship between the mode of operation and the dimensions of the junctional regions at synapses and motor end-organs. *Proc. R. Soc. London Ser. B* 148:38–56.

Edwards, F. A. (1995a). LTP: a structural model to explain the inconsistencies. *Trends Neurosci.* 18:250–255.

Edwards, F. A. (1995b). Anatomy and electrophysiology of fast central synapses lead to a structural model for long-term potentiation. *Physiol. Rev.* 75:759–787.

Faber, D. S., Young, W. S., Legendre, P., Korn, H. (1992). Intrinsic quantal variability due to stochastic properties of receptor-transmitter interactions. *Science* 258:1494–1498.

Fertuck, H. C., Salpeter, M. M. (1974). Sensitivity in electron microscope autoradiography for I-125. *J. Histochem. Cytochem.* 22:80–87.

Fertuck, H. C., Salpeter, M. M. (1976). Quantitation of junctional and extrajunctional acetylcholine receptors by electron microscope autoradiography after ^{125}I-α-bungarotoxin binding at mouse neuromuscular junctions. *J. Cell Biol.* 69:144–158.

Flucher, B. E., Daniels, M. P. (1989). Distribution of Na^+ channels and ankyrin in neuromuscular junctions is complementary to that of acetylcholine receptors and the 43 kd protein. *Neuron* 3:163–175.

Froehner, S. C. (1986). The role of the postsynaptic cytoskeleton in acetylcholine receptor organization. *Trends Neurosci.* 9:37–41.

Hall, Z. W., Sanes, J. R. (1993). Synaptic structure and development: the neuromuscular junction. *Cell* 72/*Neuron* 10(Suppl.):99–121.

Hammes, G. G. (1978). *Principles of Chemical Kinetics.* New York: Academic Press.

Hartzell, H., Kuffler, S., Yoshikami, D. (1975). Post-synaptic potentiation: interaction between quanta of acetylcholine at the skeletal neuromuscular synapse. *J. Physiol.* 251:427–463.

Heuser, J. E., Reese, T. S. (1973). Evidence for recycling of synaptic vesicle membrane during transmitter release at the frog neuromuscular junction. *J. Cell Biol.* 57:315–344.

Hines, M. (1993). Neuron: a program for simulation of nerve equations with branching geometries. *Int. J. Biomed. Comput.* 24:55–68.

Katz, B., Miledi, R. (1973). The binding of acetylcholine to receptors and its removal from the synaptic cleft. *J. Physiol.* 231:549–574.

Kruk, P. J., Korn, H., Faber, D. S. (1997). The effects of geometrical parameters on synaptic transmission: a Monte Carlo simulation study. *Biophys. J.* 73: 2874–2890.

Land, B. R., Salpeter, E. E., Salpeter, M. M. (1980). Acetylcholine receptor site density affects the rising phase of miniature endplate currents. *Proc. Natl. Acad. Sci. USA* 77:3736–3740.

Land, B. R., Salpeter, E. E., Salpeter, M. M. (1981). Kinetic parameters for acetylcholine interaction in intact neuromuscular junction. *Proc. Natl. Acad. Sci. USA* 78:7200–7204.

Land, B. R., Harris, W. V., Salpeter, E. E., Salpeter, M. M. (1984). Diffusion and binding constants for acetylcholine derived from the falling phase of miniature endplate currents. *Proc. Natl. Acad. Sci. USA* 81:1594–1598.

MacKerell, A. D., Jr., Brooks, B., Brooks, C. L., III, Nilsson, L., Roux, B., Won, Y., Karplus, M. (1998). CHARMM: the energy function and its parameterization with an overview of the program. In *The Encyclopedia of Computational Chemistry,* Schleyer, P. V. R., ed. Chichester, U.K.: John Wiley and Sons. pp. 271–277.

Madsen, B. W., Edeson, R. O., Lam, H. S., Milne, R. K. (1984). Numerical simulation of miniature endplate currents. *Neurosci. Lett.* 48:67–74.

Matsumura, K. M., Campbell, K. P. (1994). Dystrophin-glycoprotein complex: its role in the molecular pathogenesis of muscular dystrophies. *Muscle Nerve* 17:2–15.

Matthews-Bellinger, J., Salpeter, M. M. (1978). Distribution of acetylcholine receptors at frog neuromuscular junctions with a discussion of some physiological implications. *J. Physiol.* 279:197–213.

Palade, G. E., Palay, S. L. (1954). Electron microscope observation of interneuronal and neuromuscular synapses. *Anat. Rec.* 118:335–336.

Pennefather, P., Quastel, D. M. (1981). Relation between subsynaptic receptor blockade and response to quantal transmitter at the mouse neuromuscular junction. *J. Gen. Physiol.* 78:313–344.

Peters, A., Palay, S. L., Webster, H. de F. (1991). *The Fine Structure of the Nervous System: Neurons and Their Supporting Cells,* 3rd ed. New York: Oxford University Press.

Porter, C. W., Barnard, E. A., Chiu, T. H. (1973). The ultrastructural localization and quantitation of cholinergic receptors at the mouse motor endplate. *J. Membr. Biol.* 14:383–401.

Redman, S. (1990). Quantal analysis of synaptic potentials in neurons of the central nervous system. *Physiol. Rev.* 70:165–198.

Reger, J. F. (1955). Electron microscopy of the motor endplate in rat intercostal muscle. *Anat. Rec.* 122:1–16.

Robertson, J. D. (1956). The ultrastructure of a reptilian myoneural junction. *J. Biophys. Biochem. Cytol.* 2:381–394.

Rogers, A. W., Derzynkiewicz, Z., Salpeter, M. M., Ostrowski, K., Barnard, E. A. (1969). Quantitative studies on enzymes in structures in striated muscles by labeled inhibitor methods. I. The number of acetylcholinesterase molecules and of other DFP reactive sites at motor endplates, measured by radioautography. *J. Cell Biol.* 41:665–685.

Rosenberry, T. (1979). Quantitative simulation of endplate currents at neuromuscular junctions based on the reaction of acetylcholine with acetylcholine receptor and acetylcholinesterase. *Biophys. J.* 26:263–290.

Rubenstein, R. Y. (1981). *Simulation and the Monte Carlo Method.* New York: John Wiley and Sons.

Rusakov, D. A., Kullmann, D. M. (1998). Extrasynaptic glutamate diffusion in the hippocampus: ultrastructural constraints, uptake, and receptor activation. *J. Neurosci.* 18:158–170.

Rusakov, D. A., Kullmann, D. M., Stewart, M. G. (1999). Hippocampal synapses: do they talk to their neighbors? *Trends Neurosci.* 22:382–388.

Salpeter, M. M. (1967). Electron microscope autoradiography as a quantitative tool in enzyme cytochemistry: the distribution of acetylcholinesterase at motor endplates of a vertebrate twitch muscle. *J. Cell Biol.* 32:379–389.

Salpeter, M. M. (1969). Electron microscope radioautography as a quantitative tool in enzyme cytochemistry. II. The distribution of DFP-reactive sites at motor endplates of a vertebrate twitch muscle. *J. Cell Biol.* 42:122–134.

Salpeter, M. M. (1987). Vertebrate neuromuscular junctions: general morphology, molecular organization, and functional consequences. In *The Vertebrate Neuromuscular Junction,* Salpeter, M. M., ed. New York: Alan R. Liss. pp. 1–54.

Salpeter, M. M. (1999). Neurobiology: the constant junction. *Science* 286:424–425.

Salpeter, M. M., Smith, C. D., Matthews-Bellinger, J. A. (1984). Acetylcholine receptor at neuromuscular junctions by EM autoradiography using mask analysis and linear sources. *J. Electron Microsc. Tech.* 1:63–81.

Sanes, J. R., Lichtman, J. W. (1999). Development of the vertebrate neuromuscular junction. *Annu. Rev. Neurosci.* 22:389–442.

Schroeder, W., Martin, K., Lorensen, B. (1998). *The Visualization Toolkit,* 2nd ed. Upper Saddle River, N.J.: Prentice-Hall.

Shi, S. H., Hayashi, Y., Petralia, R. S., Zaman, S. H., Wenthold, R. J., Svoboda, K., Malinow, R. (1999). Rapid spine delivery and redistribution of AMPA receptors after synaptic NMDA receptor activation. *Science* 284:1811–1816.

Stiles, J. R. (1990). Acetylcholinesterase molecular forms: studies on their assay, hydrodynamic discrimination, subcellular distribution and response to neuromuscular perturbations. With: Monte Carlo computer simulations of miniature endplate currents based on the reaction of acetylcholine with acetylcholine receptor and acetylcholinesterase. Ph.D. thesis, Department of Physiology, University of Kansas.

Stiles, J. R., Bartol, T. M. (2000). Monte Carlo methods for simulating realistic synaptic microphysiology using MCell. In *Computational Neuroscience: Realistic Modeling for Experimentalists,* De Schutter, E., ed. New York: CRC Press. In press.

Stiles, J. R., Van Helden, D., Bartol, T. M., Salpeter, E. E., Salpeter, M. M. (1996). Miniature endplate current rise times <100 μs from improved dual record-

ings can be modeled with passive acetylcholine diffusion from a synaptic vesicle. *Proc. Natl. Acad. Sci. USA* 93:5747–5752.

Stiles, J. R., Bartol, T. M., Salpeter, E. E., Salpeter, M. M. (1998). Monte Carlo simulation of neurotransmitter release using MCell, a general simulator of cellular physiological processes. In *Computational Neuroscience,* Bower, J. M., ed. New York: Plenum Press. pp. 279–284.

Stiles, J. R., Kovyazina, I. V., Salpeter, E. E., Salpeter, M. M. (1999). The temperature sensitivity of miniature endplate currents is mostly governed by channel gating: evidence from optimized recordings and Monte Carlo simulations. *Biophys. J.* 77:1177–1187.

Tomita, M., Hashimoto, K., Takahashi, K., Shimizu, T., Matsuzaki, Y., Miyoshi, F., Saito, K., Tanida, S., Yugi, K., Venter, J. C., Hutchison, C. (1999). E-CELL: software environment for whole cell simulation. *Bioinformatics* 15:72–84.

Unwin, N. (1998). The nicotinic acetylcholine receptor of the Torpedo electric ray. *J. Struct. Biol.* 121:181–190.

Ventura, R., Harris, K. M. (1999). Three-dimensional relationship between hippocampal synapses and astrocytes. *J. Neurosci.* 19:6897–6906.

Wahl, L. M., Pouzat, C., Stratford, K. J. (1996). Monte Carlo simulation of fast excitatory synaptic transmission at a hippocampal synapse. *J. Neurophysiol.* 75:597–608.

Wathey, J., Nass, M. M., Lester, H. A. (1979). Numerical reconstruction of the quantal event at nicotinic synapses. *Biophys. J.* 27:145–164.

Whitaker, V. P. (1965). The application of subcellular fractionation techniques to the study of brain function. *Progr. Biophys.* 15:39–96.